Design of a Bidirectional Electric Mobility Charger for Flexible Loads Control

by

Alba Vila Suárez

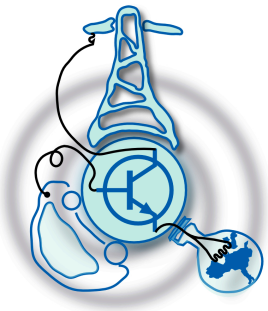

Submitted to the Department of Electrical Engineering, Electronics, Computers and Systems
in partial fulfillment of the requirements for the degree of
Master of Science in Electrical Energy Conversion and Power Systems
at the
UNIVERSIDAD DE OVIEDO
June 2022

Author .....
Alba Vila Suárez

Certified by .....
Ramy Georgious Zaher Georgious
Assistant Professor
Thesis Supervisor

Certified by .....
Matias Ariel Kippke
Gijon Smart Cities Responsible
Thesis Supervisor

Design of a Bidirectional Electric Mobility Charger for Flexible Loads Control

by

Alba Vila Suárez

Submitted to the Department of Electrical Engineering, Electronics, Computers and Systems
on June 22, 2022, in partial fulfillment of the
requirements for the degree of
Master of Science in Electrical Energy Conversion and Power Systems

Abstract

This thesis presents the design and control of a bidirectional electric vehicle charger for flexible loads control. The objective of this kind of control is to model a system that allows certain loads to inject power to the grid and contribute to stabilized and support the system. As there is power conversion, this involves the study of two different converters, one for AC-DC and one for DC-DC conversion. The topologies selected are a single-phase rectifier with Power Factor Correction (PFC) and a flyback converter. The dynamic behaviour is analyzed for both converters by obtaining the average model for both converter and the small-signal model for the flyback converter. Then, a control strategy is proposed accordingly to the studied behaviours. The equivalent first order model is also studied, and an algorithm control to preserve the battery life is implemented. A series of test are compiled, including the correct response for the different scenarios that might be presented. The tool selected to perform this tests is Simulink MATLAB®.

Thesis Supervisor: Ramy Georgious Zaher Georgious
Title: Assistant Professor

Thesis Supervisor: Matias Ariel Kippke
Title: Gijon Smart Cities Responsible

Contents

List of Figures

List of Tables

Chapter 1

Introduction

Global warming is the long-term warming of Earth's climate system that has been seen from the pre-industrial period (between 1850 and 1900) as a result of human activity, predominantly fossil fuel combustion, which increases heat-trapping greenhouse gas levels in the atmosphere [1].

Those human activities are estimated to have increased global average temperature by about 1 degree Celsius, a number that is currently increasing by 0.2 degrees Celsius per decade.

This issue has been addressed by multiple organizations and governments for several years now. The main approach these days is decarbonization, whether of transportation or power generation. In the case of the transportation, the United States Environmental Protection Agency (EPA) in 2018 estimated that the larger percentage of Greenhouse Gas Emissions in the US (28.2 %) is due to the transportation sector [2].

Moreover, there are several measurements to promote the transition into Electric Vehicles (EVs). According to the recommendations of the Electric Coalition, for example, 70 % of the travelled vehicle miles should be electric by 2040 [3]. In Spain, the Ministerio para la Transición Ecológica y el Reto Demográfico (MITECO) approved an agenda called *Plan de Recuperación, Transformación y Resiliencia* (PRTR) which states that there has to be at least 100.000 public charging points by 2023 [4].

In the case of power generation, the spanish law of climate change and energy

transition [5] contains the minimum national greenhouse gas emission reduction targets, renewable energy penetration and improvement of energy efficiency, with the main target of obtaining climate neutrality by 2050.

However, no matter how many measures and laws are put in place, the current grid system is not prepared to keep up with demand with renewable energies alone The decarbonization process with climate goals in mind is only possible by means of massive electrification. That is the reason why a new model has to be enforced, ideally, in collaboration with the consumers. But massive introduction of new electrical loads, such as vehicle charging points, may also overload the already existing infrastructures, thus a correct management of distributed energy resources must be taken into account by correctly designing control mechanisms to exchange power between loads and the low-voltage distribution network, where massive penetration is about to take place.

In the following sections, a deeper explanation of the current grid system and the proposed improvements and implementations will be performed. Following the former section, the objectives of this master's thesis will be exposed and explained with the corresponding reasoning for the decisions made in the proposed simulation model for an EV charging point.

1.1 Starting hypothesis

The biggest issue in the electrification/decarbonization process is that the actual low-voltage distribution system is not prepared to support the large introduced demand. The main reason is that renewable energies have intrinsic intermittency and non-manageability, since they are not easily stored. Deployment of large battery banks are not only expensive, but also require a large investment in logistic and the willingness from end-customers.

Nevertheless, the only feasible way to store the energy provided by renewable energies these days is through batteries. However, it would require a huge investment from the distributor companies and not really work if the demand is unknown.

The installation of smart meters, conforming advanced metering infrastructures,

enforces the idea that demand could be predictable, since peaks and valleys are frequently intercalated, intrinsically tied with working hours and human activities. For example, focusing on EV systems, if every person came back home from work and started charging their vehicle, it would create a huge demand peak that the grid would not be able to support. Even worse, it would require upgrading already existing infrastructure, increasing fixed costs for end-customers, for load peaks duration quite constrained in time.

That is why there are two charging strategies: uncoordinated strategy and coordinated strategy [6]. They are described as follows:

- Uncoordinated strategy is when EV owners charge their batteries at random, the local load increases rapidly at peak demand, resulting in significant power losses on overloaded distribution transformers and cables.

- Coordinated charging optimizes the the charging time schedule and amount of charging, avoiding the effects of high EV penetration on the grid.

If instead of instantly connecting the EV to charge when they would get home, they could make the vehicle work as if it was a portable energy storage system and inject power to the grid. One typical EV can output over 10 kW, meanwhile, the usual contracted peak power for a typical household lies between 3kW and 5kW [7].

Nevertheless, EV are not the only domestic solution. Consumers can now participate in the energy exchange thanks to the growing presence of distributed energy resources such as household photovoltaic (PV) systems with batteries and hybrid/bidirectional inverters.

This new model would make the consumers become a new concept called "prosumers". This means that the consumers not only make use of the energy, but also produce their own [8].

In a typical household, there are two types of loads, fixed a flexible. Fixed loads are those electrical loads that cannot be controlled or interrupted without affecting consumer comfort such as electric stoves, washing machines or illumination.

On the other hand, flexible loads are those that can be controlled depending on the requirements of the grid and participate in the power exchange. These kind of loads include PV installation, Energy Storage Systems (EES), EV and Heat Pumps (HP). The typical electric scheme including the aggregation of multiple of these type of loads connected to the Point of Common Coupling (PCC) with the bulk power system is shown in Figure 1-1, based on [9].

As can be seen in 1-1, electric bicycles (e-bike) and scooter are also included as electric mobility flexible loads. The reason is that, although they have less capacity than EVs, they could also work as EES on a smaller scale.

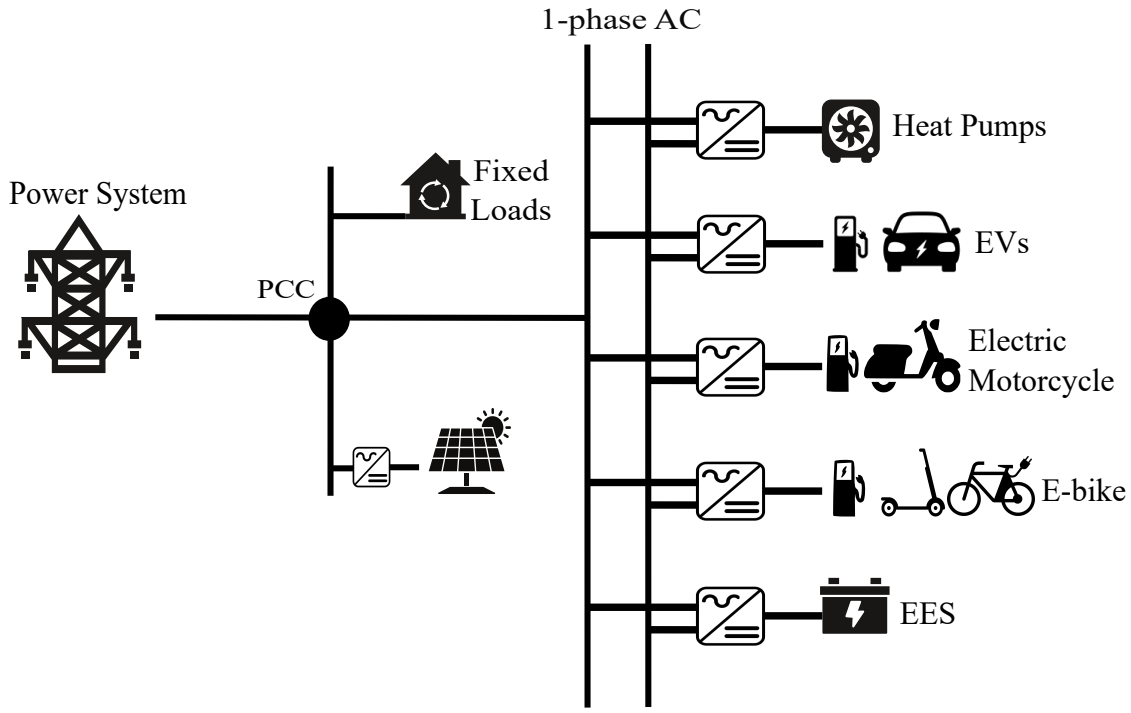

Figure 1-1: Connection of fixed and flexible loads to the power system.

However, as explained, without the development of a real-time measurement acquisition system that can accurately track energy consumption and production by renewable means, prosumers cannot be included in a previously unidirectional structure. Moreover, there are a few reasons why the system is not prepared to handle the introduction of Distributed Energy Resources (DERs) without quality control.

The addition of DERs to the grid not only opens up new opportunities for ancillary

services, but it also has the potential to degrade the Quality of Service (QoS) [9] and cause harmful effects such as: frequency imbalances, under-frequency disturbances, over-frequency disturbances or voltage sags and imbalances. Those kind of effects are not acceptable and need to be taken into account when considering the introduction of DERs to the system.

There is another point that should be make according to grid requirements, the power factor and consequently reactive power. Domestic appliances, such as microwaves or washing machines, consume reactive power which the utility is responsible for delivering. However, this kind of power is accounted for as losses in transmission lines, since it is not considered as "usable" power in the end.

Because there is no injection or pulling of reactive power, a DER with power factor equals to unity cannot offset the negative effect they are producing. That makes reactive power control a tool for increasing hosting capacities. The hosting capacity is the level of distributed generation that a circuit can support without violations requiring remediation [10]. With smart inverters, the hosting capacity of the system to support DERs will increase, since they could counteract the voltage rise from the generator by absorbing the reactive power, which would reduce the voltage.

Reactive power is best utilized when it is generated close to where it is needed. Generating reactive current at the PCC provides increased efficiency of power transfer through transmission lines and decreases transformer overloading. A vehicle can provide reactive power irrespective of the battery State of Charge (SoC). However, the charger must always be charging the battery in order to supply reactive power to the grid. In other words, if the battery has full SoC, reactive power operation is not possible [11].

In figure 1-2, the general scheme of how this charger is usually designed is shown. The AC-DC converter is connected to the grid and has as an output the DC-link. Connected to it, the DC-DC converter is found, which is, in turn, connected to the battery through a filter. This structure will be modified in the following sections to provide a bidirectional power flow according to the prosumer model that has been presented thus far.

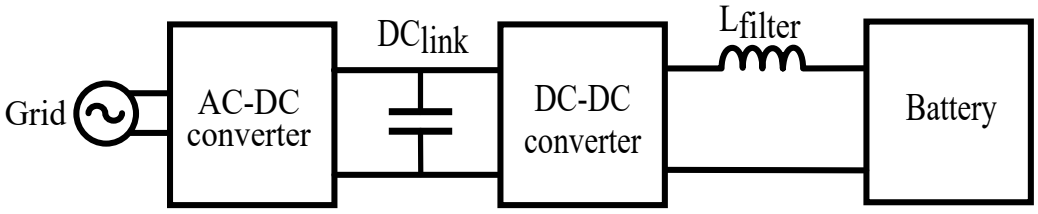

Figure 1-2: General scheme of typical used system.

In the following sections of this thesis, a state of the art analysis on the different topics that are studied in this thesis will be exposed. Then, a further behaviour analysis will be performed for both of the selected topologies. Chapter 3 contains all the details about this analysis for the single-phase rectifier converter, component design and control scheme. Chapter 4 contains the behaviour analysis of the flyback converter. It also contains the control strategy and proposed algorithms, including the measurements taken to protect and prolong battery life. After that, in Chapter 5 simulations and obtained results will be shown and observed. Lastly, in Chapter 6 conclusions based on those results will be drawn and future work will be proposed.

Chapter 2

State of Art

In order to properly explain the reasons why the topologies used in this thesis were selected, it is important to mention the different options that were also considered. In this section, the different levels and charging methods will be explained. After that, the different topologies that were studied and why the proposed ones were selected will also be explained.

Nowadays, there are three levels of EV charge whose power ranges and charging types are compiled in Table 2.1[12]. As can be seen, chargers can be classified on the basis of the power level. Currently supported power levels are AC Level 1 (3.7 kW max), AC Level 2 (22 kW max), and DC Level 3 (greater than 50 kW) [13].

Power level types	Level 1	Level 2	Level 3
Grid Voltage	230 $V_{AC}(EU)$	400 $V_{AC}(EU)$	208-600 V_{AC} or V_{DC}
Power range	$\leq$3.7 kW	3.7-22 kW	>50 kW
Charger topology	On-board	On-board	Off-board
Grid supply type	1-phase	1-phase or 3-phase	3-phase
Charging type	Slow charge	Semi-fast charge	Fast charge

Table 2.1: Power level types of charge.

Another classification that can be made is on-board chargers and off-board chargers. On-board chargers are placed inside the vehicle, so weight and size should be as reduced in size as possible. Therefore, they usually have lower power ratings (Level 1 and 2), with 1-phase AC connection. Off-board chargers are placed outside the vehicle, directly in the charging point. This allows more charging power (Level 3) as

they are not constrained by size or weight. They are usually connected to a 3-phase medium voltage AC or DC.

In Figure 2-1, the usual on-board/off-board schemes are shown, based on [14]. As can be seen, AC charging systems are usually on-board charging stations connected to the grid. On the other hand, off-board charging stations are usually DC systems in which the entire system is placed on the charging point and not the vehicle.

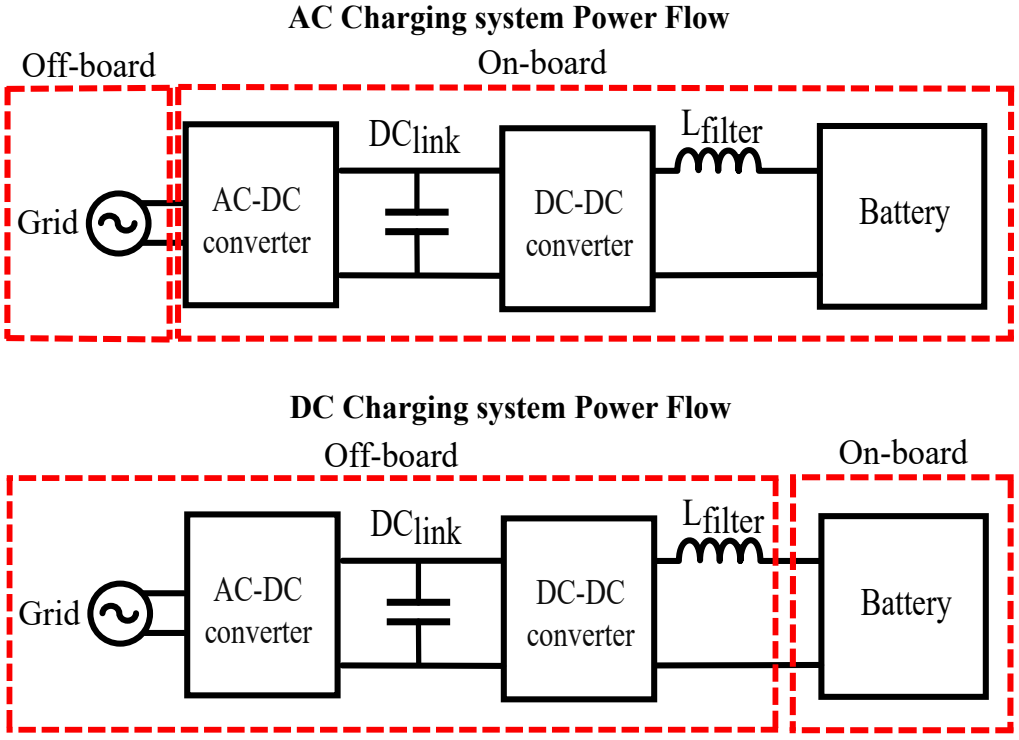

Figure 2-1: Charging system: off-board and On-board systems.

In this thesis, the focus will be on Level 1. It is a slow charge with a low power range and connected to a single phase. The topology is proposed to be on-board for the DC-DC side, as the power ratings are low and size or weight should not cause an issue. As the idea is to connect several DC-DC converters to one single AC-DC converter, that one will be placed off-board. That makes a different approach of what it was shown in Figure 2-1, since the charging system is divided at the DC-link.

Nevertheless, the idea of having off-board chargers reduced in size, weight and costs reinforces the idea that everyone can have a simple charging point at home and constitute Virtual Power Plants (VPPs) by aggregating multiple devices and

controlling them from a central platform.

Last classification that will be studied in this thesis is the charge strategy, there are five common battery charging methods [15][16]:

1. Constant voltage (CV): voltage is maintained at the maximum voltage that can be applied to the battery. The current decreases while approaching full charge. This might be effective in lower voltage settings.

2. Constant current (CC): a constant current is applied as the voltage increases to its highest value. This could cause overheating and damage, which would decrease the battery life.

3. Constant current-constant voltage (CC-CV): the charger applies a constant current until the battery reaches a certain value of voltage. Then, charging is continued at that voltage level, and current slowly decreases. It is limited to slow-charging applications [17].

4. Five-step charging pattern: it consists of a multistage constant current method. In each stage, the current is set to a certain value while voltage increases. When it reaches a certain pre-set value, the current ups to the next step. This allow faster and safer charge.

5. Pulse charging: it consists in injecting current pulses to the battery in a way that optimizes charging time but considering polarization, SoC and heating. The width and frequency of the pulses can be controlled and two methods exist: duty-fixed and duty-varied.

The proposed control strategy in this thesis is based on the CC-CV control method as it presents several advantages for the mentioned use-case. There are two main advantages: limiting charging current prevents high charging temperatures and limiting charging voltages reduce battery fading. Therefore, this method helps to extend battery life and improve safety [18]. Moreover, its the easiest method to move from charge to discharge of the battery. It will be explained in more detail in section 4.

As bidirectional charging is studied, two terms should be defined: vehicle to grid (V2G) and grid to vehicle (G2V). G2V is the typical charging point where the grid injects power and charges the battery. However, with V2G, is the battery the one injecting power. By designing the proposed kind of charger with a CC-CV control, a bidirectional charger with both G2V and V2G performance can be achieved.

2.1 Objectives

According to what has been explained in this chapter, new solutions have to be studied. In this thesis, the main objective to design a bidirectional electric mobility charger.

In order to do that, there are a few considerations that need to be taken into account. First, in order to integrate the charging point in the flexibility hub infrastructure available at the LEMUR laboratory, and given the fact that the main goal is to have a test device for power exchange with the grid, power-reduced applications are considered. Therefore, the development of this thesis will contemplate the design of a charging point for an e-bike battery (maximum 200W) instead of an EV's.

The only differences between them are actually the capacity and power ratings of the battery. However, the charging strategies are the same given they have the same technology, which means that designing a device with a much more reduced cost and topology would still be suitable for testing control schemes being used in bidirectional power exchange with the distribution grid.

By contemplating an e-bike battery, a few advantages are achieved. First, the price is much lower for the e-bike battery. Second, the testing time of charge and discharge is lower, which is good in a laboratory environment considering the goal of the investigation. This model also reduces complexity, another advantage in a testing environment. Lastly, as will be explained further on, the topologies that will be selected will not really affect the behaviour of the system. They will be scalable or interchangeable without impacting the main control structure.

Something else to consider, as previously mentioned, is that power factor control is

important in DERs because of reactive power. In this thesis, a power factor correction will be included in the design. However, the objective in this case will be to maintain the power factor equal to 1 to avoid the possible negative effects.

Considering all of the aforementioned starting points, the initial design can be proposed. As the charger will be connected to the grid, two different stages are necessary. In this case, the topology structure is based on two stages, an AC-DC converter and a DC-DC converter.

As shown in Figure 2-2, the bidirectional AC-DC converter is connected to the grid, which will make the off-board part of the system. The output of this is a DC-link capacitor that is, in turn, the input of the bidirectional DC-DC converter. For control strategy purposes that will be further explained, the output of the DC-DC converter is connected to the battery through an inductive filter. This will make the on-board part of the charging system.

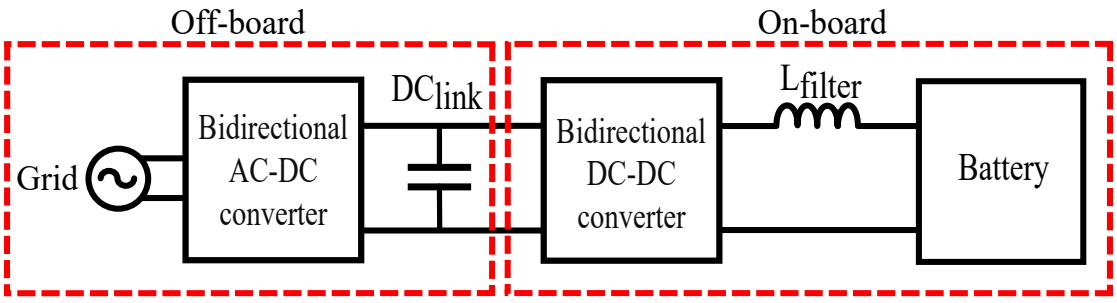

Figure 2-2: General scheme of the proposed system.

As previously mentioned, e-bike batteries have lower power ratings than EV's ones. Because of that, the DC-DC converter will need a lower power rating than the AC-DC converter could be able to provide. Because of that, the structure shown in Figure 2-3 is proposed. To avoid wasting power and lower costs, it could be possible to connect multiple DC-DC converters to a single AC-DC converter. This will have to be further studied once the topologies are selected and power ratings are known.

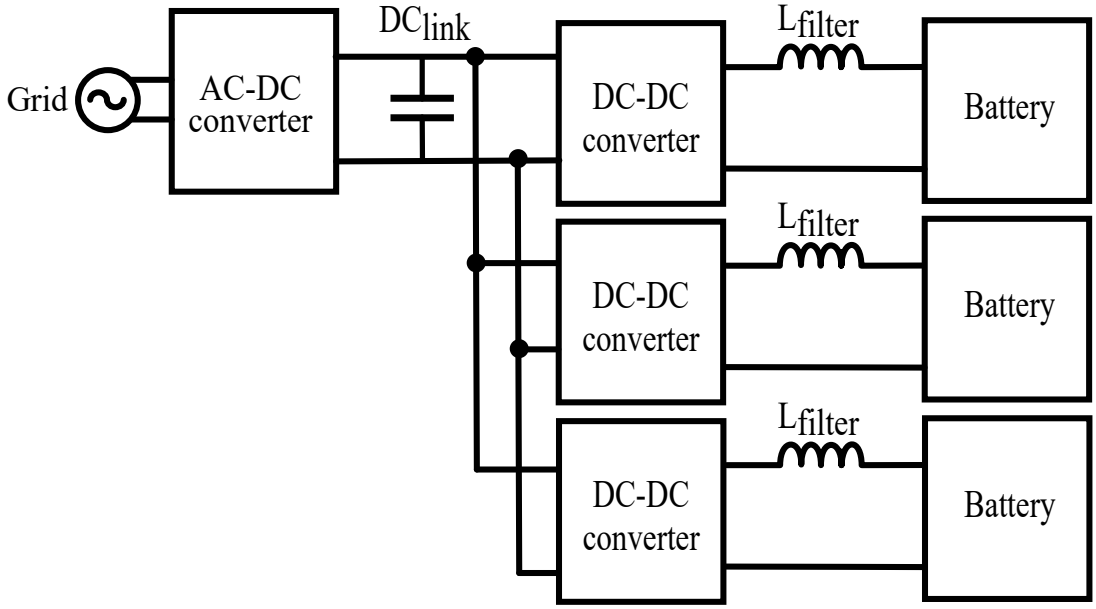

Figure 2-3: Scheme of one AC-DC converter and multiple DC-DC converters connected to it.

2.2 AC-DC converter

For the AC-DC converter, there are two viable choices: half-bridge converter and full-bridge. The half bridge topology shown in Figure 2-4 has fewer components and lower cost, but exhibits high component stresses. However, full-bridge systems shown in Figure 2-5 have more components and higher cost, with lower component stresses [19].

Then, in this case, as the final goal is to build a physical model, the most viable choice is the full-bridge single-phase rectifier with Power Factor Correction (PFC). The power ratings are very wide depending on the component design and the control strategy and modulation are fairly simple. The selected power of this topology is 1kW. As the maximum rating of the DC-DC converter is around 200 W, up to 5 converters could be connected to one single AC-DC converter.

As explained, the AC-DC converter will have to provide some kind of power factor correction to the system to avoid compromising the quality of service.

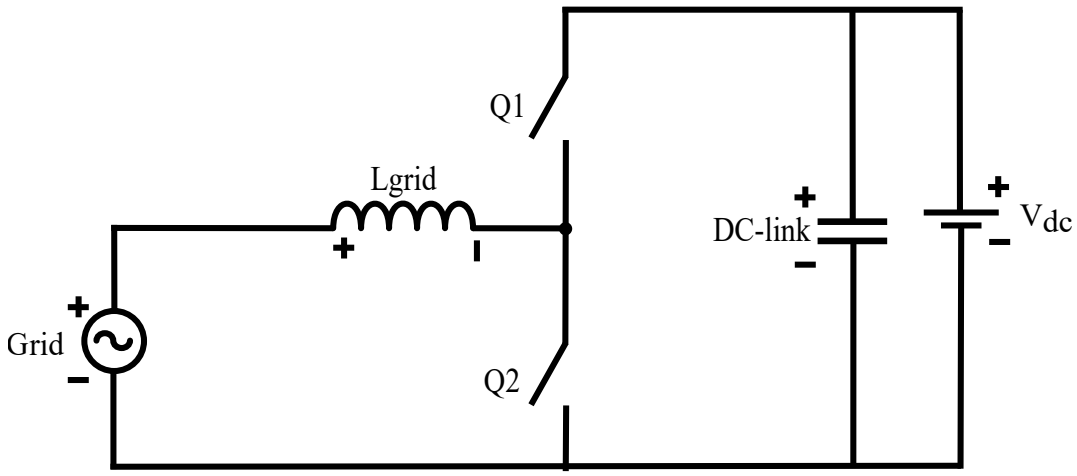

Figure 2-4: Half-bridge converter topology.

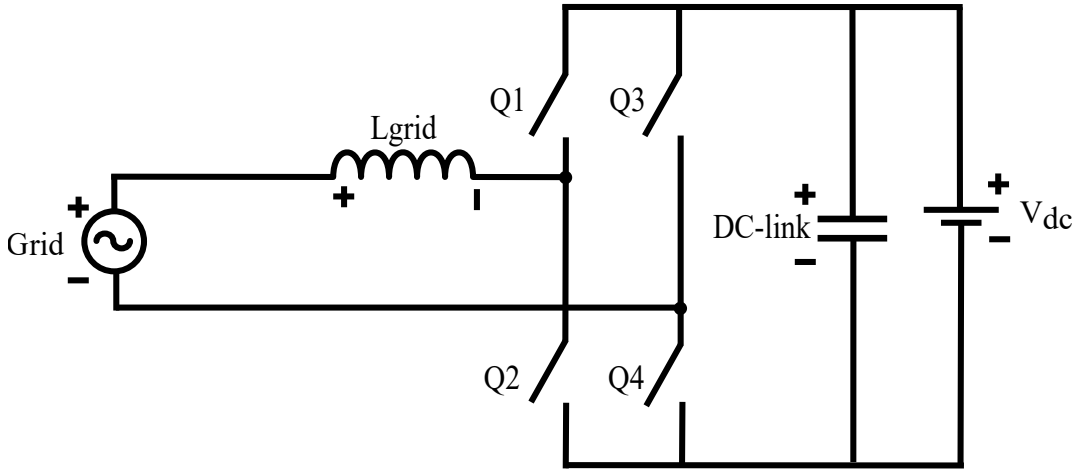

Figure 2-5: Full-bridge converter topology.

2.3 DC-DC converter

Now, in the case of the DC-DC side, there are three topologies studied for this thesis as an option. Those topologies are: buck-boost converter, dual active bridge (DAB) converter and flyback converter.

The bidirectional buck converter topology is shown in Figure 2-6. This topology is known because of its flexibility and simplicity. It could be used at any power rating

by scaling the components and its efficiency is decently high (>90%) [20]. However, in this case, it is beneficial in this case to have an isolated topology, which means a galvanic isolated transformer.

Galvanic isolated topologies are necessary to increase the security for end-users. Moreover, since the voltage is stepping-down from 400V to 40V, in order to do it in a single stage without stressing the switching devices, it is better to have an additional design element. In this case, the transformer adds the relation between primary and secondary.

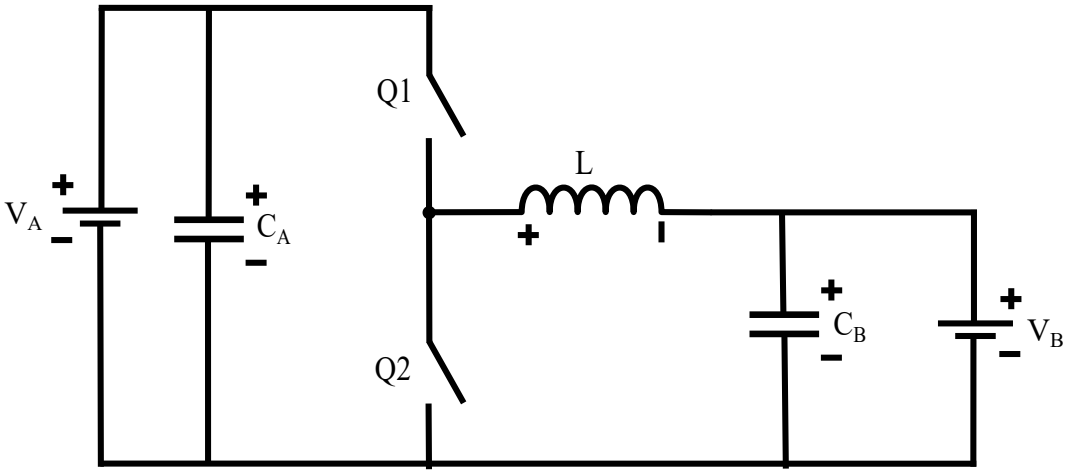

Figure 2-6: Bidirectional buck converter topology.

The bidirectional buck-boost topology is shown in Figure 2-7 [21]. The difference between the buck-boost topology and the buck topology is that the buck only allows the output to have lower voltage rating while in the buck-boost the voltage of any side could be higher or lower. However, as previously mentioned, the buck-boost converter does not have galvanic isolation, which makes it not suitable for this operation.

The DAB converter topology is shown in Figure 2-8. This converter is usually used in higher power ratings (in the order of kW), and its efficiency is usually around 98% [22]. This converter is also isolated because of the included transformer. However, its control is based on a phase-shift and it would be more difficult that for the other proposed topologies.

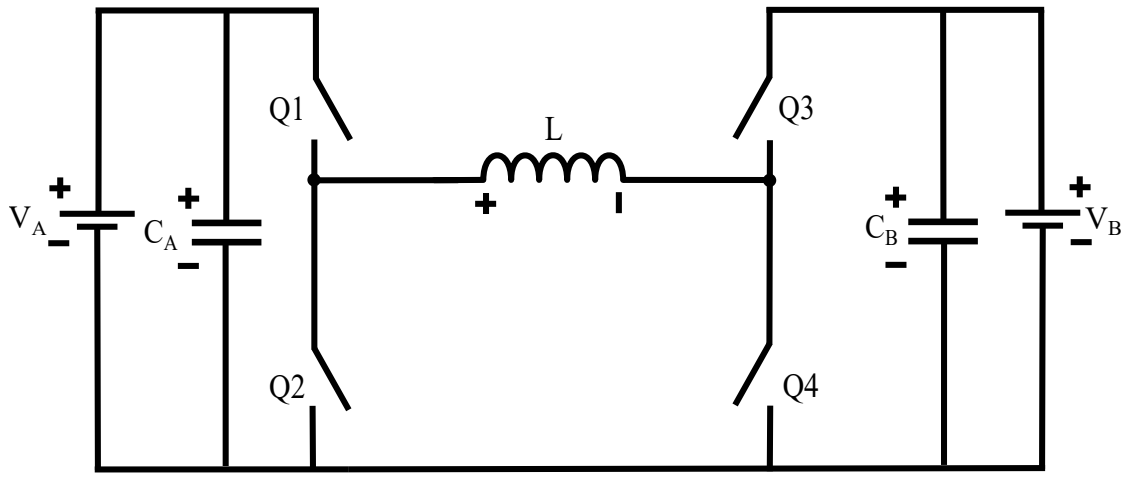

Figure 2-7: Bidirectional buck-boost converter topology.

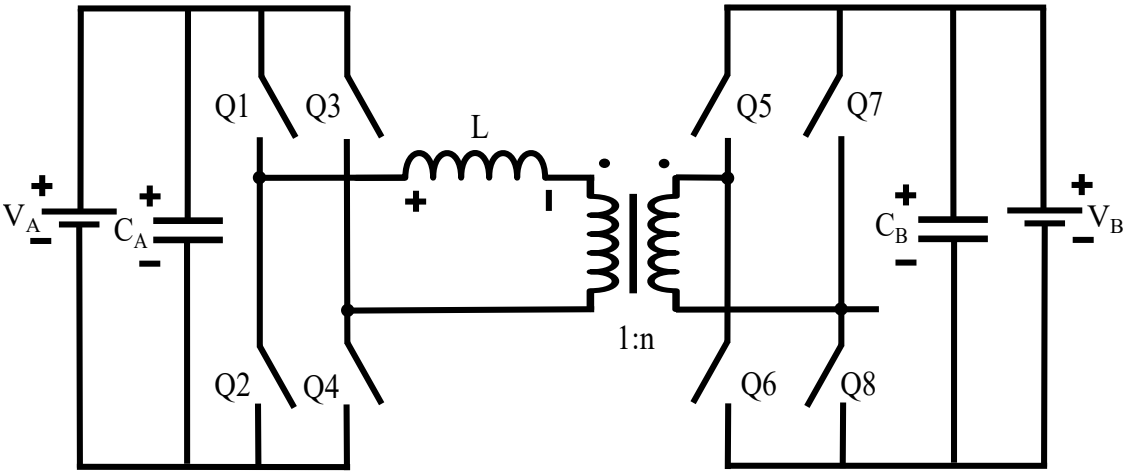

Figure 2-8: Dual Active Bridge converter topology.

Another option to consider are the inductor–inductor–capacitor (LLC) resonant converters, which are the most attractive due to its high efficiency, low electromagnetic interference (EMI) emissions, a wide operation range, and the ability to achieve high power density. However, they are difficult to analyze and design because of its multiple resonant components and various operation modes [23]. The LLC topology is shown in Figure 2-9 [24].

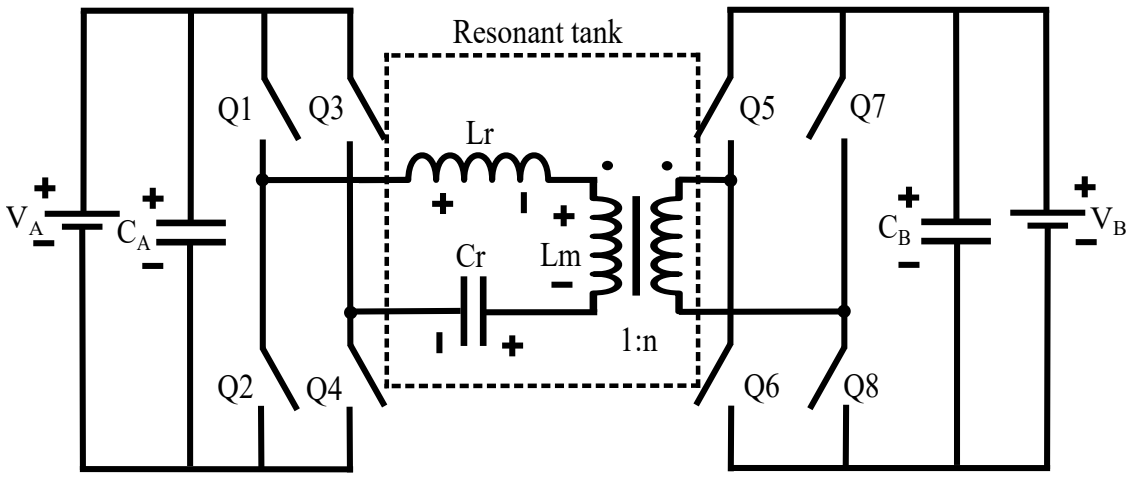

Figure 2-9: LLC converter topology.

Last option is the flyback converter, which is shown in Figure 2-10. This converter is isolated and easy to control. However, its main drawbacks are that its power ratings are usually around 200 W maximum, and its efficiency is approximately 80% [25].

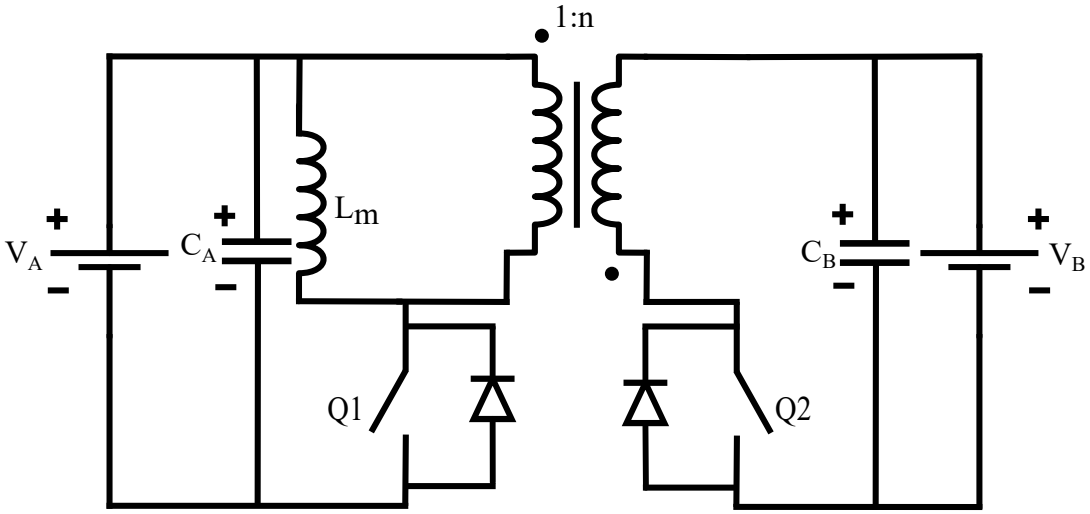

Figure 2-10: Flyback converter topology.

Finally, as DC-DC converter, the proposed topology is a bidirectional flyback converter. This topology has a few drawbacks, as mentioned before, such as low rated power ($\approx$ 200 W) and low efficiency. However, as the proposed future work is to physically implement this charger, a lower power rating and lower price is view

as an advantage. In addition, the transformer allows the converters to achieve much higher or lower values of the DC voltage transfer function than their transformerless counterparts [25].

To perform test in the future physical model, it is an advantage to be able to use an electrical bicycle battery instead of an electrical vehicle one. The reasons for this include lower price, lower charging and discharging times and a smaller size.

As the electrical bicycle and electrical vehicle both use a Li-ion battery, the type of charging and discharging will not be affected by the capacity or power ratings of the battery. It will simply have to be scaled for a higher value battery capacity and power in the case of the EV.

Moreover, taking into account the general scheme explained before, this converter is completely exchangeable. This will be explained in more detail further on.

For the reasons mentioned above, a flyback converter with a rated power of 200 W will be studied. The battery selected in this case is the Bosch PowerPack 300 model [26].

Chapter 3

AC-DC Rectifier/Inverter Converter with PFC

As explained before, the proposed topology is a controlled single-phase converter that can work as rectifier or inverter. The topology is shown in Figure 3-1, where the grid side can be assumed to be an AC voltage source or a resistance and the load side can be assumed to be a load resistance or a DC voltage source, depending on whether it works as a rectifier or inverter, respectively.

This topology is formed by an L filter connected to the grid side, four switching devices, a DC-link capacitor and a load that is represented by resistance calculated from the rated power of the converter. The proposed switching frequency in this case is 10 kHz.

The are a few switching devices that could be used in this case. The proposed ones are IGBTs. The reason for this is that the R_{ON} resistance are typically lower that the MOSFET's ones, which will simplify the behaviour analysis. Also, as the selected switching frequency is 10 kHz there is no need for a MOSFET device, which are usually more expensive.

The rated power of this converter is selected as 1 kW. The reason is that, as mentioned before, the typical flyback converter rated power is about 200 W. With a 1 kW rectifier converter, four to five flyback converters could be connected.

In the following subsection, the average model will be obtained to shorten com-

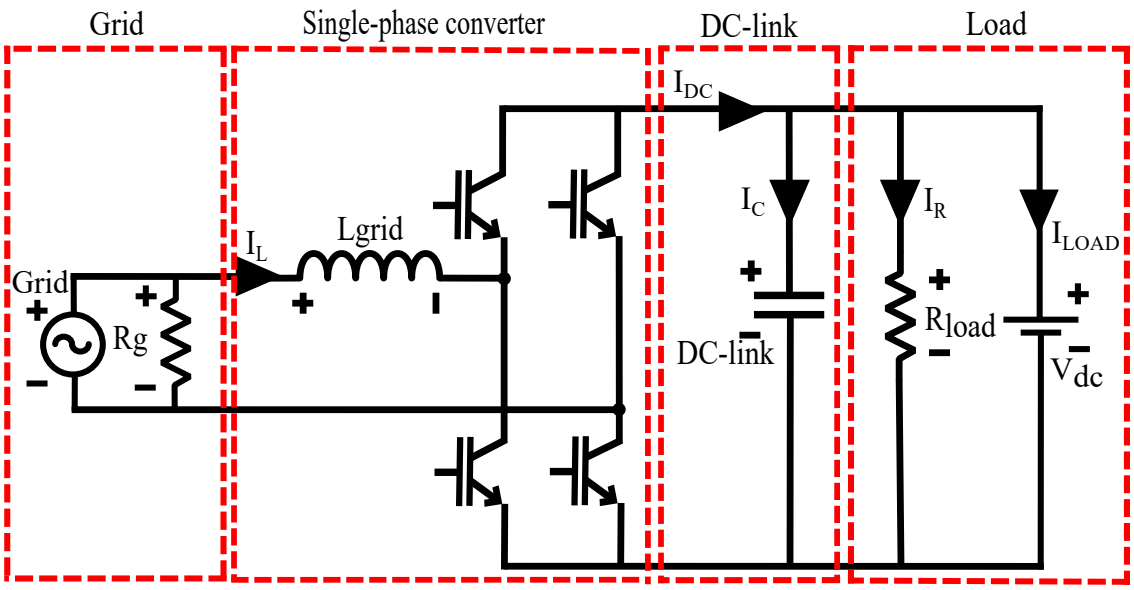

Figure 3-1: Single phase rectifier switching model

putational time. Then, the component design of the single-phase rectifier will be performed. Lastly, the proposed control strategy will be explained.

3.1 Average Model

To obtain the average model of this topology, is easier if studied as an inverter. To do that, the DC-link voltage is assumed to be set by a voltage source. The connection to the grid is substituted by a resistor Rg with a high value so that it does not consume too much current.

The starting single-phase inverter is shown in Figure 3-2. The entire process to obtain the average model is explained in more detail in Appendix A.

$$V_{inv} = (2D - 1)V_{DC} \tag{3.1}$$

$$I_{DC} = (2D - 1)I_L \tag{3.2}$$

From (3.1) and (3.2), the obtained average model is represented in Figure 3-3, where D is the duty cycle of the inverter. In this figure it can be seen both converter

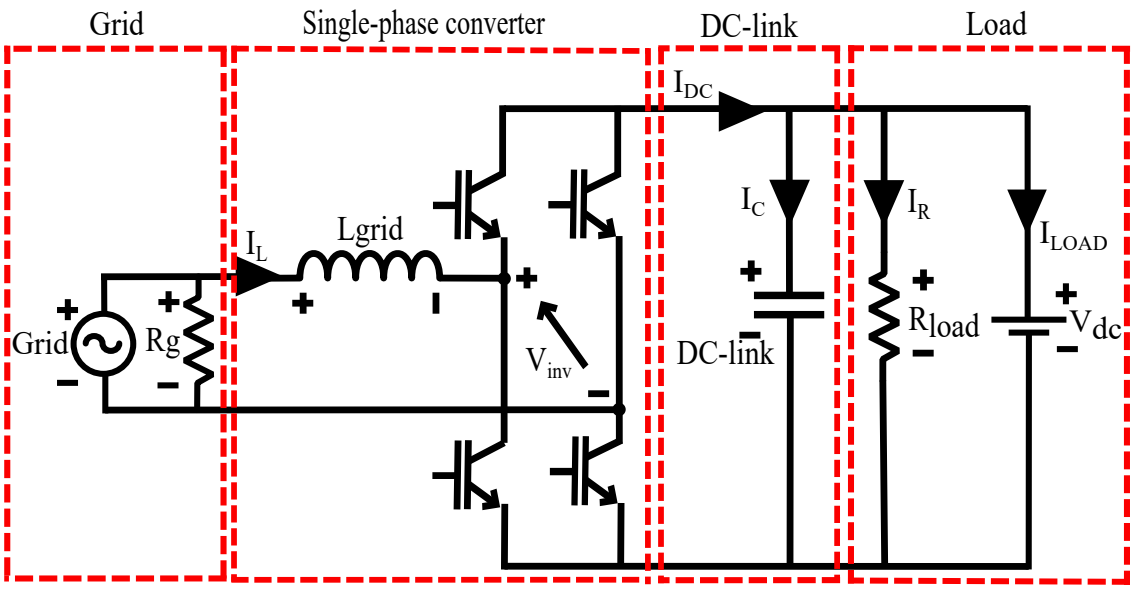

Figure 3-2: Single phase rectifier model to analyze dynamic behaviour

options. It could as an inverter by assuming the grid side to be a Rg resistor and the DC voltage source in the load side. But it could also work as a rectifier by assuming that the grid side is connected to the actual grid and the load side is a R_{load} resistor.

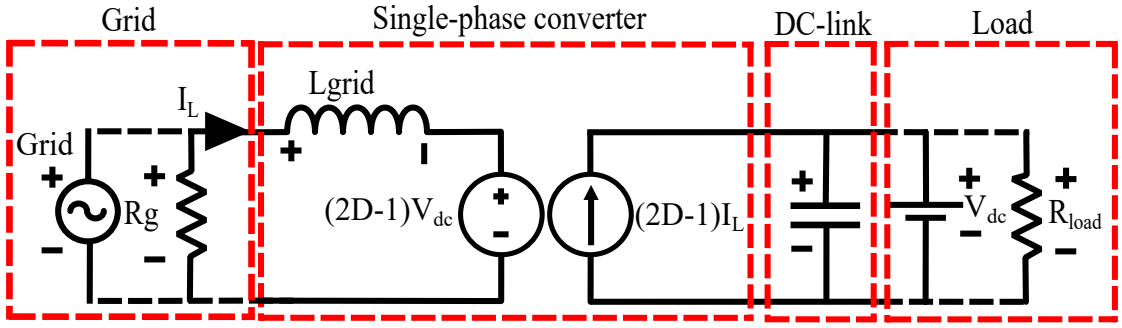

Figure 3-3: Single Phase Rectifier average model

3.2 Component Design

As explained, the first step is to design the components of the converter. To do that, Table 3.1 collects the initial data.

From Table 3.1, the data needed to obtain the components values is extracted and

Parameter	Data	Value	Units
Rated power	P	1	kW
Grid voltage	V_{grid}	230	V_{rms}
Grid frequency	f_{grid}	50	Hz
DC-link voltage	$V_{DC_{link}}$	400	V
Switching frequency	$f_{switching}$	10	kHz

Table 3.1: Input data of the rectifier converter.

the following process is carried to determine said values.

First, the size of the inductor filter is calculated. The worst case scenario is taken into account, and a ripple of 20% is selected.

Equation (3.5) will be used for the Kirchoff's analysis. The rms and peak current values of the inductor are calculated with equations (3.3) and (3.4). With this values, an inductor of 6.09 mF is obtained, as can be seen in equation (3.6).

$$I_{rms} = \frac{P}{V_{grid_{rms}}} = \frac{1000}{230} = 4.3478A \tag{3.3}$$

$$I_{peak} = \sqrt{2} \cdot I_{rms} = 6.15A \tag{3.4}$$

$$V_L = L \cdot \frac{di}{dt} \tag{3.5}$$

From 3.5, where V_L is the difference of the nominal value of the inductor voltage and the minimum one in one period.

$$400 - 325 = L\frac{6.15 \times 20\%}{1/(10 \times 10^3)} \rightarrow L = 6.09mH \tag{3.6}$$

In order to calculate the size of the capacitor the characteristic equation (3.7) will be used. To obtain the load resistor value, the worst case scenario is taken into account, which in this case is the maximum rated power. The R_{load} is calculated by (3.8).

$$\frac{V_{DC}^2}{R_{load}} \cdot t = \frac{1}{2}C(V_{DC}^2 - V_{min}^2) \tag{3.7}$$

$$P = \frac{V_{DC}^2}{R_{load}} \rightarrow 1000 = \frac{400^2}{R_{load}} \rightarrow R_{load} = 160\Omega \tag{3.8}$$

As can be seen in (3.9) a capacitor of 657.89 μF is obtained, where V_{min} is the selected minimum voltage value through the capacitor.

$$\frac{400^2}{160} \times 0.01 = \frac{1}{2}C(400^2 - 360^2) \rightarrow C = 657.89\mu F \tag{3.9}$$

All these values are collected in Table 3.2. To make sure that the design values will not be affected once the physical model is implemented because they are far from the commercial values, the RS Component[27] inventory was checked. The commercial values are also shown in Table 3.2. As these values are not really far from the design ones, the behaviour will not be not affected by this in the physical model.

Data	Value	Units	Commercial Value	Units
L_{grid}	6.09	mH	6	mH
R_{load}	160	Ω	160	Ω
$C_{DC_{link}}$	657.89	μF	680	μF

Table 3.2: Calculated components of the rectifier converter

To study the behaviour of the single-phase converter, it is easier to do it while it works as an inverter. Thus, the analysis is initiated from the grid point of view and continued by analysing the rest of the nets by Kirchhoff's analysis. Because of that, to test the correct behaviour of the average model, a sinusoidal reference is introduced in both switching and average model, which will provide the duty cycle. The component values design in this section are introduced into the model as well.

The current and voltage are then measured in the Rg resistor, and the dynamic behaviour of the two models is represented in Figure 3-4. As can be seen, both models have the same behaviour and produce a sinusoidal waveform according to the reference.

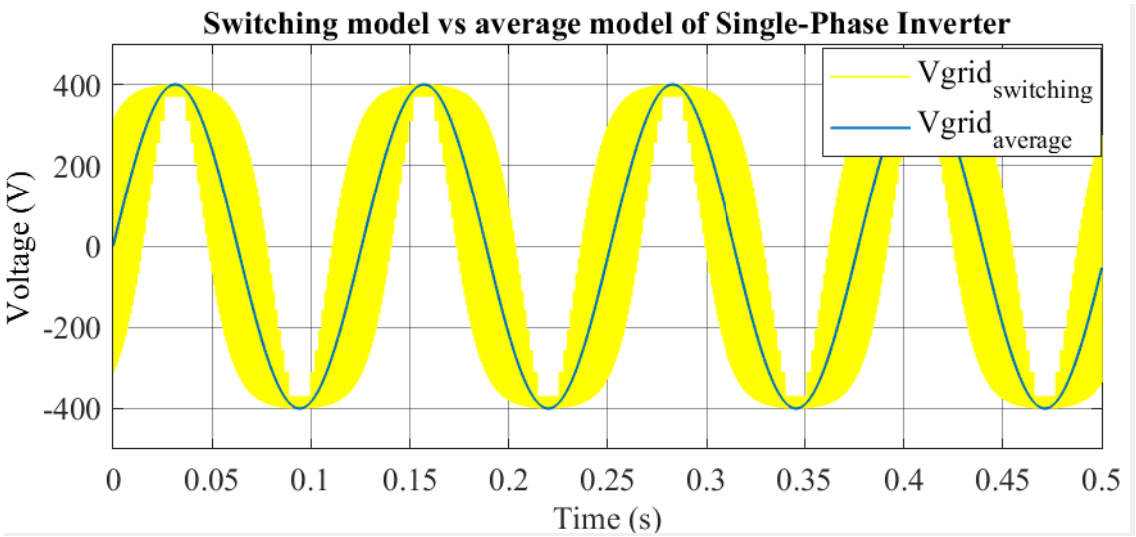

Figure 3-4: Single Phase Rectifier switching model vs. average model.

3.3 Control Scheme

The system's control has been split in two cascaded loops: DC-link voltage control loop being the outer loop and grid current control loop being the inner loop. Current control is necessary to make sure that unity power factor is achieved (grid current and voltage are in phase) and to limit the current to the maximum values that are fixed by the power rate. The DC link voltage control is used to keep the DC link voltage at a fixed value.

The target is the indirect control of the active power exchange between the grid and the inverter and this is done by the voltage control. For instance, when more power is demanded, the DC-link voltage will decrease and more power from the grid will be consumed in order to keep this voltage constant and also feed the inverter. Same happens in the situation where the battery is feeding the grid, it increases the voltage in the DC-link and power will be consumed by the grid. That relationship is shown in 3.10.

Considering the inverter has no losses, the generated power is assumed to be the grid power. The load power is considered to be the DC-DC converter connected as a load, which will require the same power as the battery.

$$P_{DC_{link}} = P_{generated} - P_{load} \tag{3.10}$$

Both control structures interact in a cascade architecture in which the inner control loop is the current control and the outer control loop is the voltage control, as shown in Figure 3-5. Finally, the PWM modulator generates the signal for the IGBT control following an unipolar strategy.

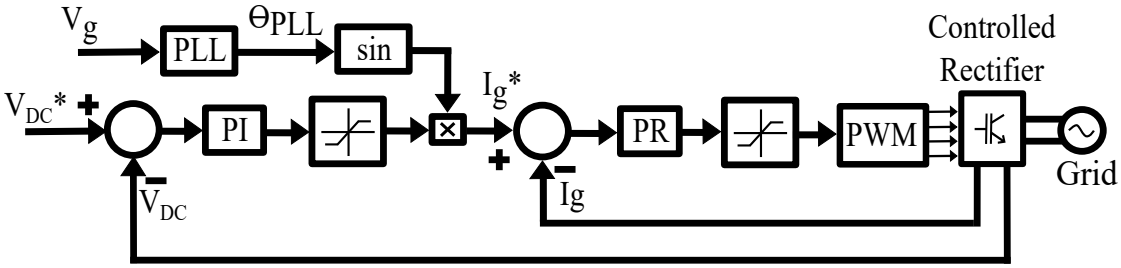

Figure 3-5: Control scheme of the Single-Phase rectifier

3.3.1 Current Control

Two options have been checked for the current control. The first one is the utilization of a synchronous reference frame rotating at grid frequency Proportional-Integral PI controller and the second one is based on the utilization of a proportional resonant controller (PR).

The first option has the advantage of and easier regulator tunning and it adapts to frequency changes in the grid. However, in single phase, some extra steps need to be made for applying Park and Clarke transformations.

The second option avoids this extra steps and it does not add too much tunning difficulties. The regulator values will be fixed, so it will be designed to have the best performance at grid frequency. Although it may seem as a drawback, the grid is assumed to be strong enough so that no significant frequency variations would be expected.

Finally, the PR option has been selected due to its adaptability to the requirements and the conditions and its lower complexity.

The plant considered for the current regulator tunning has been an L circuit, whose values come from the inductive filter. The control scheme is shown in Figure 3-6, where PEC stands for Power Electronic Converter and represents the controlled rectifier whose dynamics are neglected do to the Bandwidth (BW) difference and assumed to be ≈ 1.

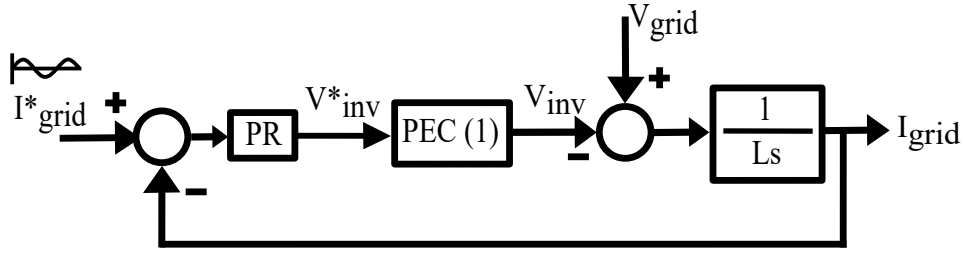

Figure 3-6: Current control scheme

The PR controller transfer function is shown in (3.12), where the regulator denominator is fixed by the grid angular frequency ($\omega_g = 2\pi 50$).

$$PR(s) = K_{pi}\frac{(s+z_1)(s+z_2)}{s^2+w_g^2} \tag{3.11}$$

In order to do the tunning of the PR controller, there are two possible methods: root-locus approximation and 2^{nd} order approximation by PI controller.

- **Root-locus approximation method:**

In this method, as the numerator has two zeros, one of them is used for cancelling the plant's pole at $-1/L$ and the other is used for the current bandwidth (BWc) selection. Said BW is selected as 300 Hz, which is far enough from the switching frequency.

$$PR(s) = K_{pi}\frac{(s+z_1)(s+z_2)}{s^2+w_g^2} \tag{3.12}$$

As the poles in closed loop will follow a circular trajectory whose center is the remaining zero, it is placed at 150 Hz, half the value of the current bandwidth. The target is to achieved a critically damped system, in other words, the fastest damped system for the given conditions.

In Figure 3-7 the root locus representation of the control system is shown for a more clearer explanation. From the root locus, the gain value, K_{pi}, can be known using MATLAB. As explained, the system is critically dumped, which means the K_{pi} is placed in the real axis of the root locus. MATLAB will show the selected value at any of the points of that axis as the user will desire faster or lower response.

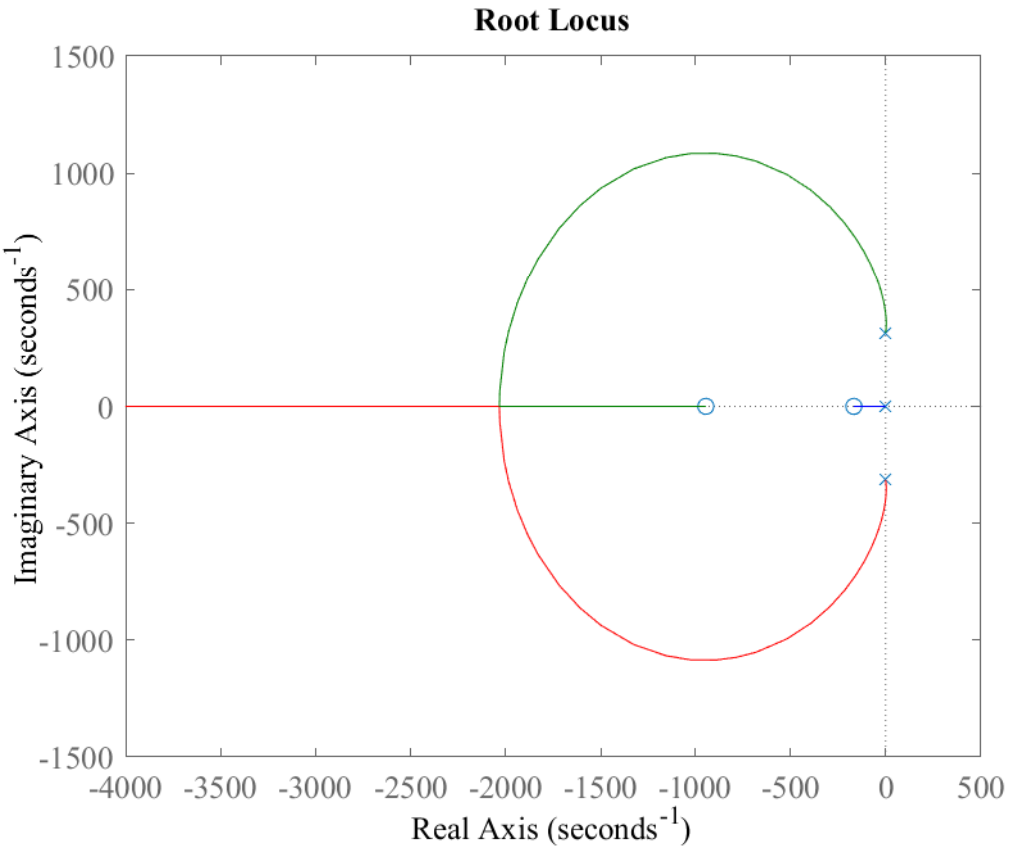

Figure 3-7: Current control root locus

- **2^{nd} order approximation by PI controller:**

In this method, the assumption is that the transfer function of the PR controller is based on a PI controller but adapted to a specific frequency. Starting by the PI

transfer function in parallel form and equating (3.13) and (3.14), the resulting k_p and k_i are shown in (3.15) and (3.16).

$$TF(s) = \frac{PI(s)G(s)}{1 + PI(s)G(s)} = \frac{(k_p + \frac{k_i}{s})(\frac{1}{Ls})}{1 + (k_p + \frac{k_i}{s})(\frac{1}{Ls})} = \frac{\frac{k_p}{L}s + \frac{k_i}{L}}{s^2 + \frac{k_p}{L}s + \frac{k_i}{L}} \tag{3.13}$$

$$TF(s) = \frac{2\zeta w_n s + w_n^2}{s^2 + 2\zeta w_n s + w_n^2} \tag{3.14}$$

$$\frac{k_p}{L} = 2\zeta w_n \rightarrow k_p = 2\zeta L w_n = 2\zeta L 2\pi BW_c \tag{3.15}$$

$$\frac{k_i}{L} = w_n^2 \rightarrow k_i = w_n^2 L = (2\pi BW_c)^2 L \tag{3.16}$$

With that, the parallel form of the PR controller as a function of the PI transfer function is shown in (3.17).

$$\begin{aligned} PR(s) &= k_p + \frac{k_i}{s + jw_g} + kp + \frac{k_i}{s - jw_g} = \frac{k_p s + jw_g k_p + k_i}{s + jw_g} + \frac{k_p s - jw_g k_p + k_i}{s - jw_g} = \\ &= \frac{(k_p s + jw_g k_p + k_i)(s - jw_g) + (k_p s - jw_g k_p + k_i)(s + jw_g)}{(s + jw_g) + (s - jw_g)} = \\ &= \frac{2k_p s^2 + 2k_i s + 2w_g^2 k_p}{s^2 + w_g^2} = 2k_p(\frac{s^2 + k_i/k_p s + w_g^2}{s^2 + w_g^2}) = 2k_p(1 + \frac{k_i/k_p s}{s^2 + w_g^2}) \end{aligned} \tag{3.17}$$

By equating (3.17) with (3.15) and (3.16), the final PR controller is shown in (3.18).

$$PR(s) = 8(\zeta L \pi BW_c)(1 + \frac{\frac{\pi BW_c}{\zeta}s}{s^2 + w_g^2}) \tag{3.18}$$

To test the differences between the two tunning methods, first the values of both of them will be compared. Then, a reference current step will be introduced in the control system to see the different responses.

The values of both of the PR designs are shown in Table 3.3. As can be seen, the values are in the same order in both cases. Therefore, although the response might be expected to be slightly different, it should not make a big difference.

Data	Root Locus	2^{nd} order
K_p	30.81	45.23
K_i	$3.42 \cdot 10^4$	$2.13 \cdot 10^4$

Table 3.3: Calculated values of the PR controller.

Now, the response changes between those two methods in the transient of the grid current. This response in shown in Figure 3-8. As can be seen, they are pretty similar, but the 2^{nd} order approximation method one has a lower transient peak. This method is selected for the following test, as it can be seen that the system follows the current reference exactly.

To improve the response in the current control and avoid saturation, a feedforward system has also been implemented. The control architecture used in this case is shown in Figure 3-9.

The grid voltage (V_{grid}) has been feedforwarded and then normalized by dividing it by the DC-link voltage value ($V_{DC_{link}}$). That gives a duty cycle values between -1 and 1, so it also has to be normalized to have values between 0 and 1. This control loop provides the response shown in the PR tunning method comparison, Figure 3-8.

3.3.2 Synchronous Reference Frame Phase Lock Loop (SRF-PLL)

Once the current control is working, in order to jump up to the DC-link voltage control, a PLL is necessary. Voltage control will produce the current reference to the inner loop. However, this reference comes from a (PI) control action, and it represent the peak value of the sinusoidal current.

As explained, power factor correction needs to be implemented in this thesis to avoid affecting the grid. For now, the power factor will be set to be = 1. However, with this power factor it will not be able to offset the negative effects on the grid.

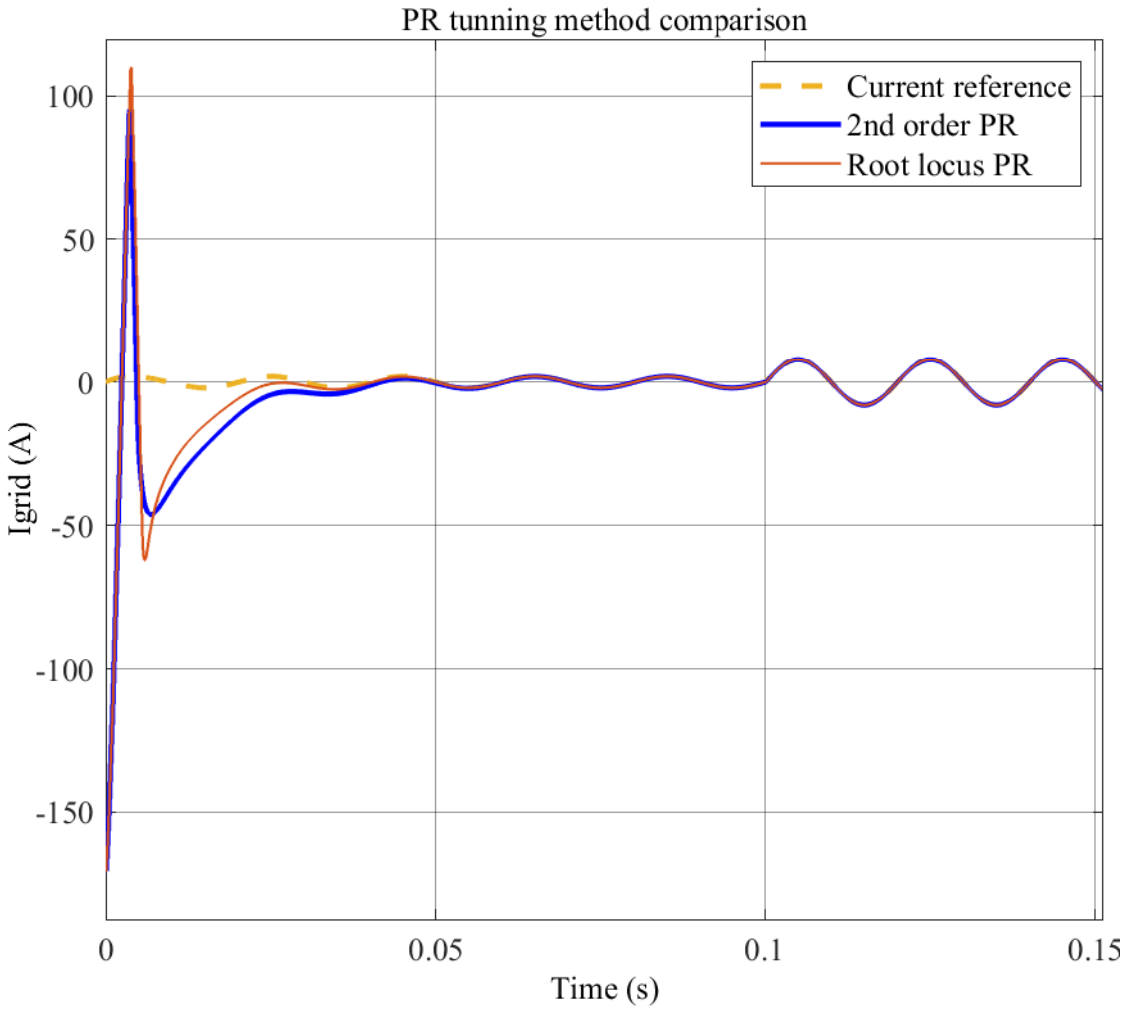

Figure 3-8: PR tunning methods comparison

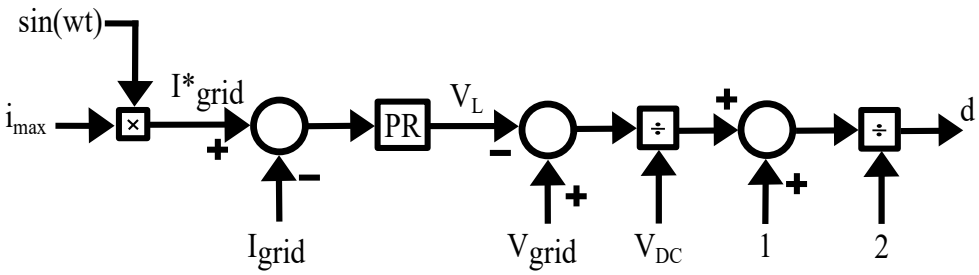

Figure 3-9: Control loop architecture with feedforward.

Then, the current control reference is a sine waveform in phase with the grid voltage as zero reactive power exchange is desired in this case. Therefore, the peak value coming from the DC voltage controller needs to be transformed into a sine wave

at grid frequency. This frequency is calculated using a PLL.

As it was commented before, a PLL in single phase requires some additional effort for applying Park transformation. For this implementation a quadrature signal generator (QSG) is used. The QSG consists in a transfer function that generates an orthogonal output with respect to the input. QSG's transfer function results in the equation (3.19):

$$QSG(s) = \frac{s - \omega_g}{s + \omega_g} \tag{3.19}$$

Being $\omega_g = 2\pi 50$ for the expected grid. Once the orthogonal signal is obtained, the Park transform can be performed. The quadrature component is divided by the the direct one to avoid interference if the voltage magnitude changes. The resultant value is fed into a PI that will track the input frequency. PI's transfer function structure is shown in (3.20).

This PI's output is feedforwarded with the expected grid frequency in order to reduce the initial tracking time. Finally, the phase angle is obtained by using a integrator and it is feedbacked to the Park transformation closing the loop. A global scheme for this PLL is shown in Figure 3-10 (a).

$$PI(s) = K_{pPLL}\frac{s + K_{iPLL}}{s} \tag{3.20}$$

PI's tunning is done by 2^{nd} order approximation considering the control scheme in Figure 3-10 (b). The plant considered is just a pole in the origin, $1/s$. Then, the coefficients K_{pPLL} and K_{iPLL} are obtained for a 25Hz BW and critical damped system ($\zeta = 1$) as shown in (3.21) and 3.22.

$$K_{pPLL} = 2 \cdot \zeta \cdot BW_{PLL} \tag{3.21}$$

$$K_{iPLL} = \frac{BW_{PLL}^2}{K_{pPLL}} \tag{3.22}$$

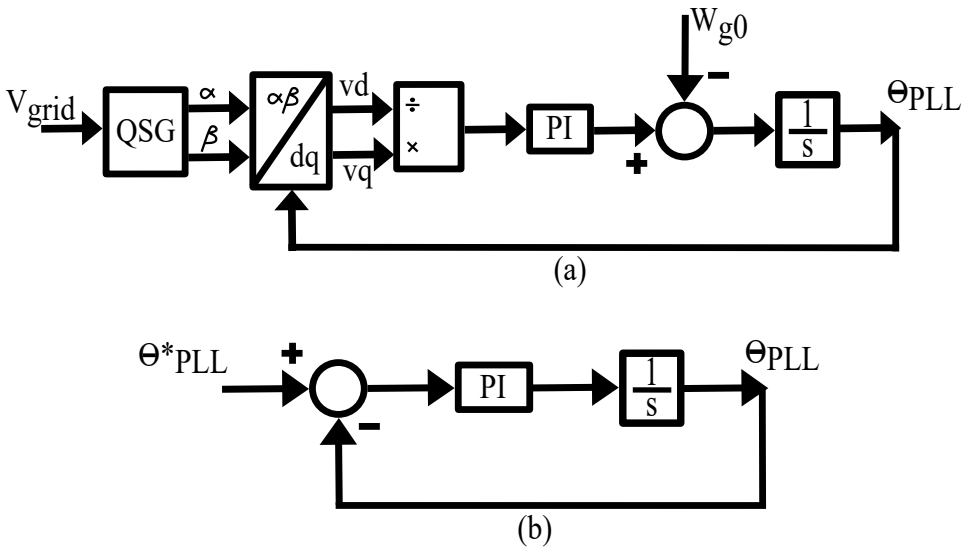

Figure 3-10: (a) PLL scheme (b) Control diagram for the PLL's PI tunning.

3.3.3 Voltage control

The voltage control deals with DC magnitudes, thus, a common PI regulator can be used in this case. The control scheme results in Figure 3-11, considering the system plant as a capacitor. As the current sensor measures output current, if the DC link controller has to increase the DC link voltage, the output grid current has to increase.

The tunning method selected is the second order approximation. The damping factor is chosen as 1 (critically damped) and the BW selected is 5 Hz. This BW is more than 10 times lower than the one in the inner control loop.

The PI structure is the same as mentioned before and its coefficients are calculated in the same way, as in (3.23) and (3.23). However, as previously said, a simple capacitor plant is considered.

$$K_{pv} = 2 \cdot \zeta \cdot BW_v C_{DC_{link}} \tag{3.23}$$

$$K_{iv} = \frac{BW_v^2 C_{DC_{link}}}{K_{pv}} \tag{3.24}$$

From the equations stated above, the following values for the voltage PI controller

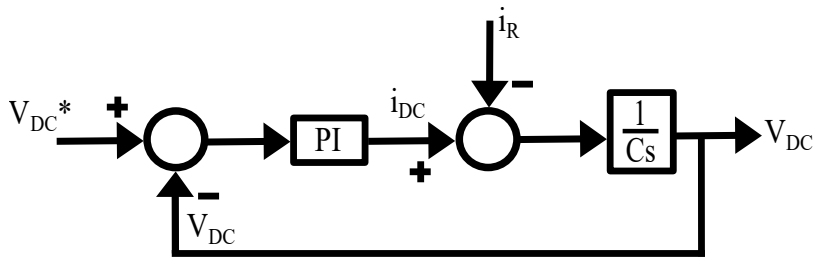

Figure 3-11: Voltage Control

were obtained as shown in Table 3.4.

Data	Value
BW_v	5 Hz
Kp_v	0.04
Ki_v	15.7

Table 3.4: Voltage PI controller parameters

To improve the behaviour of the system and avoid saturation, the current reference is divided by the maximum voltage value before is multiplied by the sinusoidal reference, as shown in Figure 3-12.

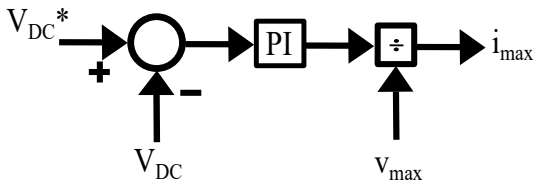

Figure 3-12: Voltage Control with Saturation

The first thing than needs to be tested is the correct stabilization of the DC-link voltage. To do that a $R_{load} = 500\ \Omega$ is connected to the output. A reference voltage with a ramp configuration was introduced in the system, with the DC-link already charge to 180 V. In a physical model, this would be done by introducing a bypass and charging the DC-link before starting the control loop.

In Figure 3-13, it can be seen that the DC-link voltage follows the ramp reference exactly in less than 0.5 seconds. Plus, the initial transient does not have a high peak

value that could damage the converter components.

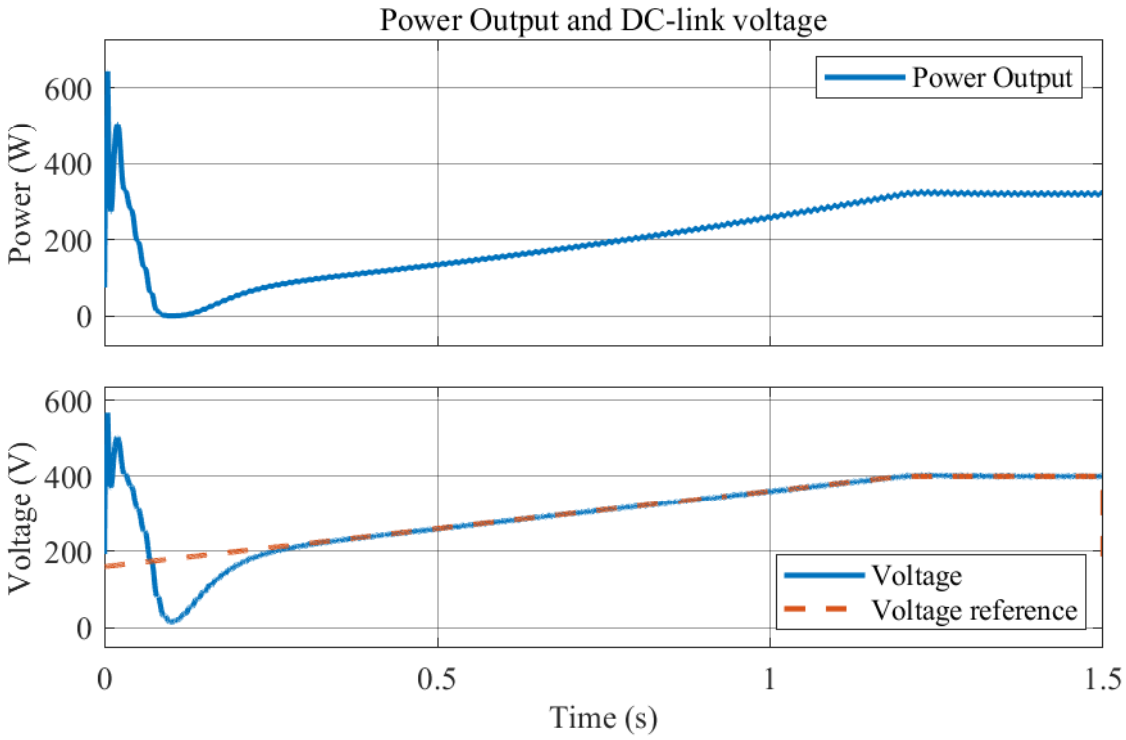

Figure 3-13: DC-link voltage for a fixed value resistor load.

Chapter 4

Flyback Converter

As explained before, the selected topology is a bidirectional flyback whose schematic is shown in Figure 4-1, where: V_{dc} is the voltage at the DC-link, V_{bat} is the voltage of the battery, i_p is the primary side current, i_m is the current flowing through the magnetizing inductance, i_s is the secondary side current, i_c is the current flowing through the filter capacitance, i_R is the current flowing through the load resistor, n is the turns ratio of the transformer and D is the duty cycle of the primary side MOSFET and D' is the duty cycle of the secondary side one.

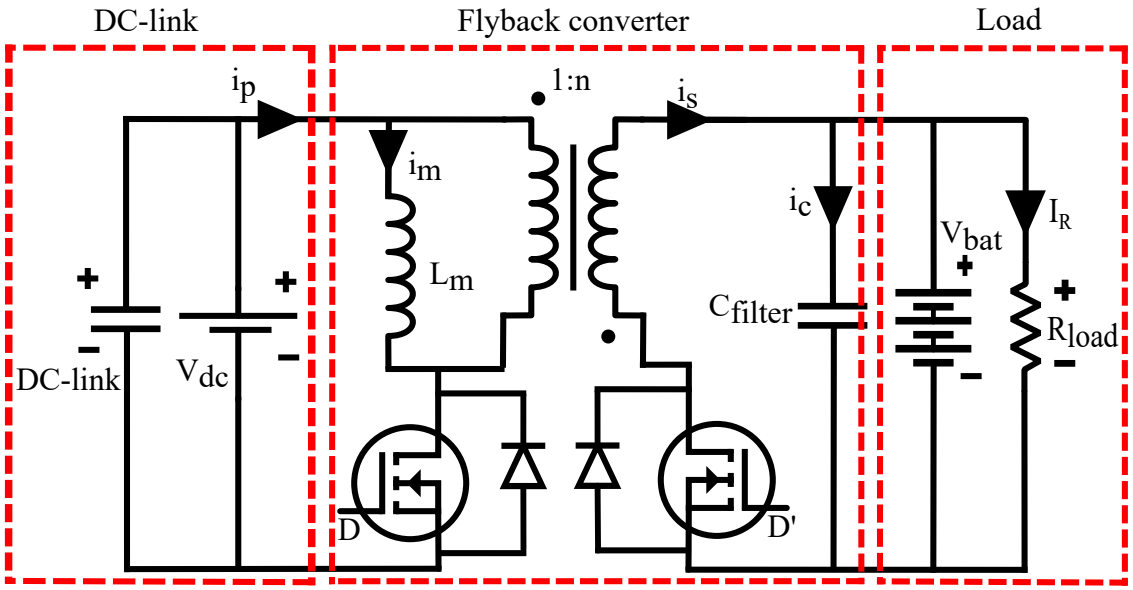

Figure 4-1: Bidirectional flyback converter.

In this case, the switching frequency is selected as 100 kHz because of the design of the components. With higher switching frequency, the smaller the components will be. It usually induces higher losses, but efficiency is not the scope of this thesis.

Then, the proposed switching devices are MOSFETs. The reason for that is that they usually support higher switching frequencies and have higher efficiency at lower voltage levels.

As can be seen in Figure 4-1, the DC-link side can be assumed to be a capacitor controlled by the AC-DC Converter or a DC voltage source in order to test the flyback converter. In this case, to maintain the voltage fixed, the voltage source will be considered from now on. On the load side, a simple resistor or the battery could be connected. The resistor will be assumed to be the load while studying the dynamic behaviour of the converter. However, the control strategy will be tested with the first order battery model that will be explained further on.

In this section, the entire process to control said flyback converter will be explained. To do that, first, the value of the components must be obtained. After that, it will be explained how to control the power exchange since it is a bidirectional converter.

Once that is done, the next steps are obtaining the average model and the small-signal model. The reason to obtain those models is that, while they have the same dynamic behaviour as the switching model, they require less computational time.

4.1 Power Flow of the Converter

As explained before, the flyback converter will be the one in charge of the direction of the power flow. That means that the control of the power flow of this converter has two different modes: charge (G2V) and discharge (V2G). Selecting between those two modes is as simple as changing the duty cycle, D, above or below a critical value, D_{crit}, whose value is calculated as shown in (4.1).

$$D_{crit} = \frac{1}{\frac{V_{dc}}{V_{bat}}n + 1} = \frac{1}{\frac{400}{42} \times \frac{1}{4} + 1} = 0.2308 \tag{4.1}$$

In the first case, when the battery is charging, the duty cycle will be above the critical one ($D > D_{crit}$), and the current will flow as shown in Figure 4-2.

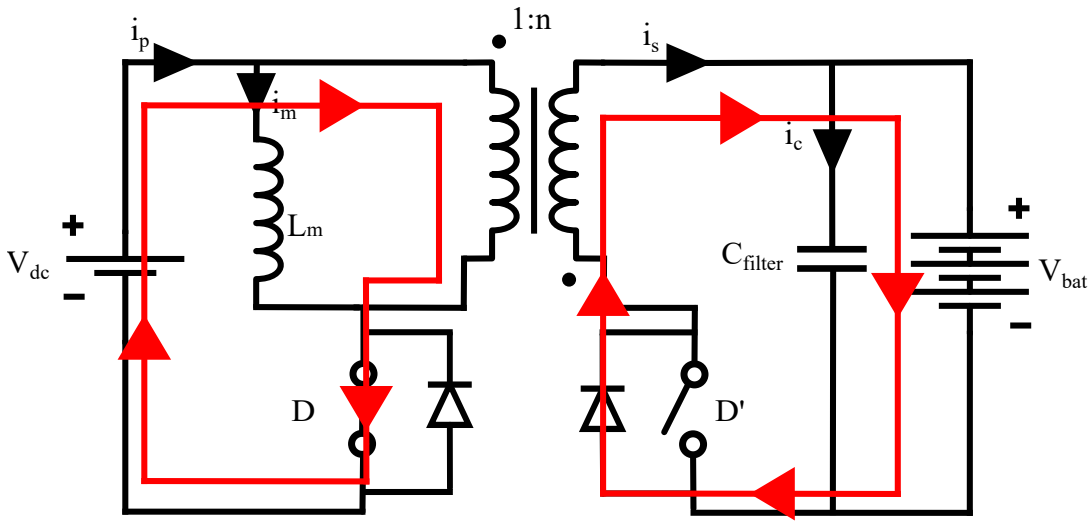

Figure 4-2: Power flow charging the battery (G2V).

In the second case, when the battery is injecting power to the grid, the duty cycle will be below the critical value ($D < D_{crit}$), and the current will flow as shown in Figure 4-3.

4.2 Converter Design

Now that the topology is selected, a few components must be designed depending on the maximum power that it is going to achieve. In this case, the selected power is going to be the maximum recommended for this kind of topology, 200 W.

The components mentioned before are the turns ratio of the transformer, the magnetizing inductance and the filter capacitor. It is important to clarify that, in this case, the turns ratio is defined by $n = N2/N1$.

Another important aspect to mention is that in order to design the components

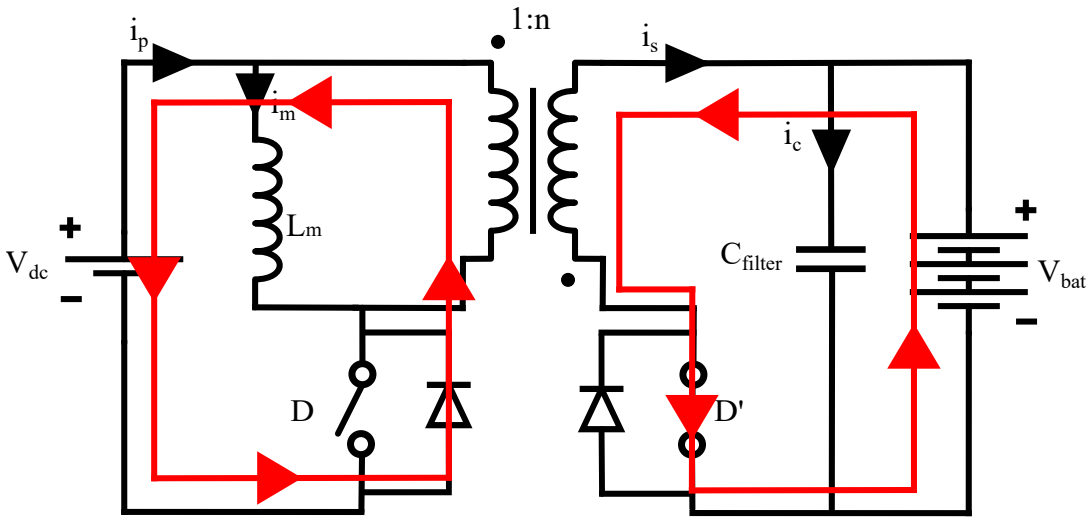

Figure 4-3: Power flow discharging the battery (V2G).

of this topology, as it is a bidirectional flyback, both charge and discharge modes are taken into account. This means that the calculated values must comply with the requirements according to the input and output values of both modes.

Parameter	Data	Value	Units
Rated power	P	200	W
DC-link voltage	V_{dc}	350 - 400	V
Battery voltage	V_{bat}	30 - 42	V
Battery current	I_s	0.10 - 4	A
Voltage ripple	V_{ripple}/V_{bat}	$\leq$1%	V

Table 4.1: Input data for flyback components design.

Initial design values are shown in Table 4.1, where V_{ripple} is the voltage ripple selected in this case. Considering this data and following the calculation procedure in Appendix B, the final equations to determine the components values are shown in (4.2),(4.3) and (4.4). That procedure contemplates, as explained, both charge and discharge scenarios. In this case, the most constrictive scenario is the discharge mode, so the following values are based on that.

$$L_{m_{min}} = \frac{n^2 \cdot R_{l_{max}} \cdot (1 - D_{crit})^2}{2 \cdot f_s} = \frac{4^2 \times 420 \times (1 - 0.2308)^2}{2 \times 100 \times 10^3} = 19.9\ mH \qquad (4.2)$$

$$C_{min} = \frac{D_{max} V_{out}}{f s R_{L_{min}} V c_{pp}} = 214.28\ \mu F \tag{4.3}$$

$$L_f = \frac{(\Delta I_o/100) V_{bat}}{(\Delta I_o/100) I_o 2\pi f_s} = \frac{(1/100) \times 37.5}{(1/100) 4 \times 2\pi 100 \cdot 10^3} = 0.150 \mu H \tag{4.4}$$

The calculated values for the different components of the flyback are compiled in Table 4.2. Said values will be used to determine the dynamic behaviour of the flyback converter.

Same as with the single-phase rectifier, the commercial values were checked to make sure they would not become a problem in the physical model. As can be seen in Table 4.2, the design values are not far from the commercial ones, so this will not affect the behaviour either.

Parameter	Data	Value	Units	Commercial Value	Units
Turn ratio	n	1/4			
Magnetizing inductance	L_m	20	mH	20	mH
Filter capacitance	C_{filter}	214.28	μF	220	μF
Filter inductance	L_{filter}	15	μ H	15	μH

Table 4.2: Values of the flyback components.

4.3 Average model

As explained before, the first step to obtain the transfer function of the converter is to obtain the average model, which has the same behaviour as the switching model but requires much less computational time. This is helpful testing the charge and discharge of the battery because it requires long simulations that will take a lot of time simulating the switching model.

The process to obtain the average model is explained in Appendix C, from where (4.5), (4.6), (4.7) are extracted by collecting the DC terms of the inductance equation. In those relations, L_m is the value of the magnetizing inductance and R_s is the series resistance of the MOSFETs.

$$L_m \cdot \frac{di_m(t)}{dt} + i_m \cdot R_s = D \cdot V_{dc} - D' \cdot \frac{V_{bat}}{n} \tag{4.5}$$

$$i_p = D \cdot i_m(t) \tag{4.6}$$

$$\frac{D' \cdot i_m(t)}{n} - \frac{V_{bat}}{R_{bat}} = 0 \tag{4.7}$$

Also, it is important to point out two important relationship in this process. The first one is the relation between D and D', which is shown in (4.8). Also, the value of R_s in this process depends on the duty cycle equilibrium point, the turns ratio and the ON resistance of the MOSFET (Ron) following the relationship shown in (4.9).

$$D' = 1 - D \tag{4.8}$$

$$R_s = R_{on}(D + \frac{D'}{n^2}) \tag{4.9}$$

From said equations, the average model is obtained as shown in Figure 4-4.

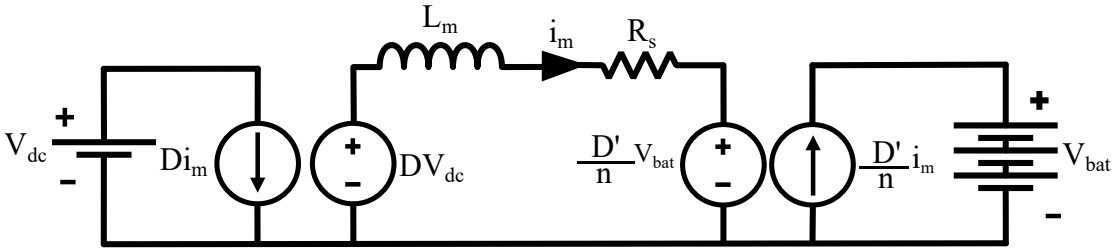

Figure 4-4: Bidirectional flyback converter average model.

4.4 Small-signal model

Next step is to build the small-signal model. In order to simplify, the battery has been assumed to be just a resistor that will fix the demanded power value, as explained at the beginning of this chapter.

This is based on the idea that the analysis can be equally done by replacing the

battery by it's equivalent as a resistor. However, the small-signal analysis will give different circuits, depending if we are analysing the buck behaviour (G2V) or the boost behaviour (V2G).

Same as with the average model, the entire process is further explained in Appendix C. From there, collecting the 1^{st} order terms of the inductor, capacitor and input current equations, equations from (4.10) to (4.12) are obtained.

$$\begin{aligned} L_m \frac{d\widehat{i}(t)}{dt} = D \cdot \widehat{v_{dc}}(t) - \frac{D'}{n}\widehat{v_{bat}}(t) + \widehat{d}(t)(V_{dc} - I \cdot R_{on} + \frac{I \cdot R_{on}}{n^2} + \frac{V_{bat}}{n}) \\ - \widehat{i}(t)(D \cdot R_{on} + \frac{D' \cdot R_{on}}{n^2}) \rightarrow \end{aligned} \tag{4.10}$$

$$L_m \frac{d\widehat{i}(t)}{dt} = D \cdot \widehat{v_{dc}}(t) - \frac{D'}{n}\widehat{v_{bat}}(t) + \widehat{d}(t)V_{ss} - \widehat{i}(t)R_s$$

$$C \ \frac{d\widehat{v_{bat}}(t)}{dt} = \frac{D'}{n}\widehat{i}(t) - \frac{I}{n}\widehat{d}(t) - \frac{\widehat{v_{bat}}(t)}{R_{bat}} \tag{4.11}$$

$$\widehat{i_p}(t) = D \cdot \widehat{i}(t) + I \cdot \widehat{d}(t) \tag{4.12}$$

From said equations, the electric scheme shown in Figure 4-5 can be extracted, where V_{ss} is a constant whose value is $V_{ss} = V_{dc} - I \cdot R_{on} + I \cdot R_{on}/n^2 + V_{bat}/n$.

From Figure 4-5 and taking into account that dependent voltage and current sources with the same ratio constitute ideal DC transformers, the small-signal model is obtained as represented in Figure 4-6.

As can be seen, this model is also dependent of the duty cycle equilibrium point. The difference is that the average model is a linear model, but the small-signal model is not. This means that, to obtain the same values in steady-state, the equilibrium point should be dynamic in the small-signal case, and change in each iteration.

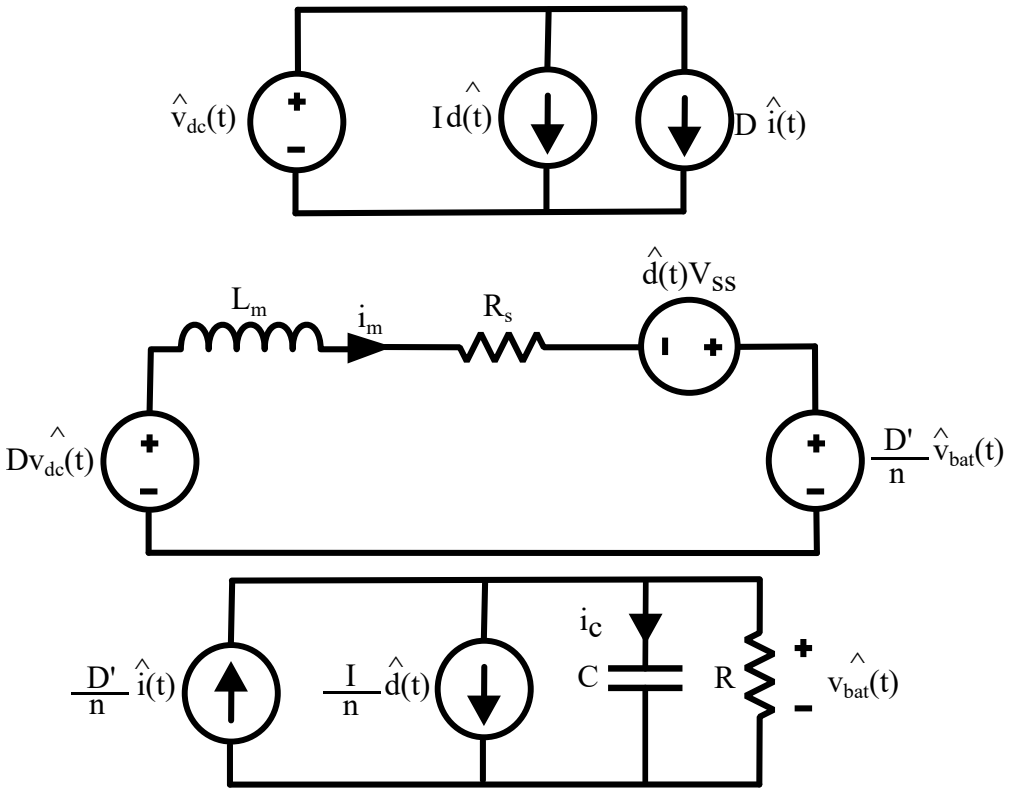

Figure 4-5: Bidirectional flyback converter small-signal model.

This scenario will not be tested in this thesis because the only interest is the dynamic behaviour. To perform the simulations in the following sections, the average model will be used.

This behaviour can be seen in Figure 4-7 and Figure 4-8. As expected, both switching model and average model have the same dynamic behaviour and steady-state values. However, the small-signal has a steady-state error, while maintaining the same dynamic behaviour as the other two models.

Also, as seen in Figure 4-7 and Figure 4-8, by applying a small change in the duty cycle at 0.1 seconds, the time response of the flyback output voltage and current reach a steady-state value at 0.12 seconds approximately.

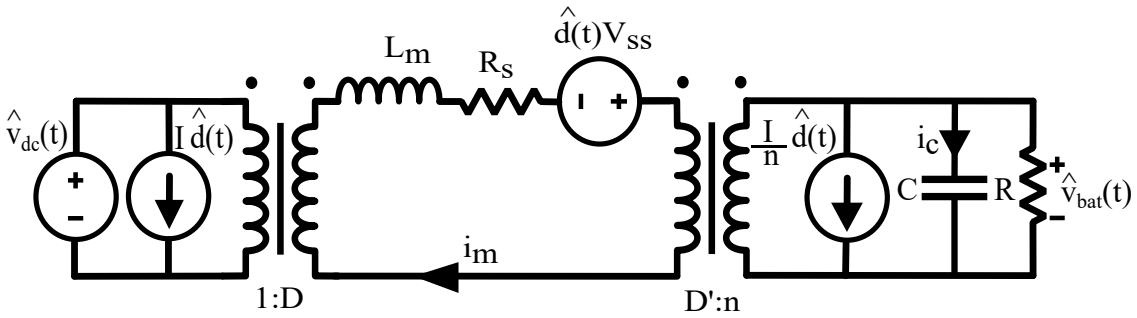

Figure 4-6: Small-signal model of bidirectional flyback converter with ideal DC transformers.

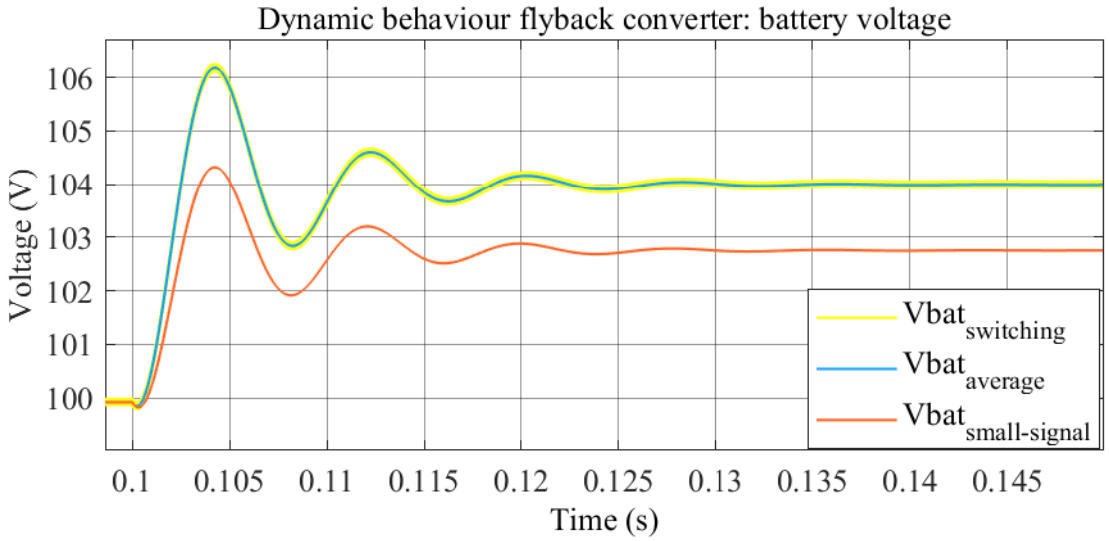

Figure 4-7: Time response to a small change of the duty cycle of the flyback converter: battery voltage.

4.5 Control strategies

The proposed control strategy in this thesis is based on the constant current-constant voltage (CC-CV) control method, since it is the traditional one for lithium batteries [28]. This strategy's main drawback is that it is not compatible with fast-charging, but that is not a purpose of the proposed EV charger as this is focused on domestic charging which is typically slow charge.

The main idea of the CC-CV control strategy is that it is based on two stages. In stage 1, the charger applies a constant current to the battery until it reaches the cut-off voltage (maximum voltage value). Then, the charging continues at stage 2,

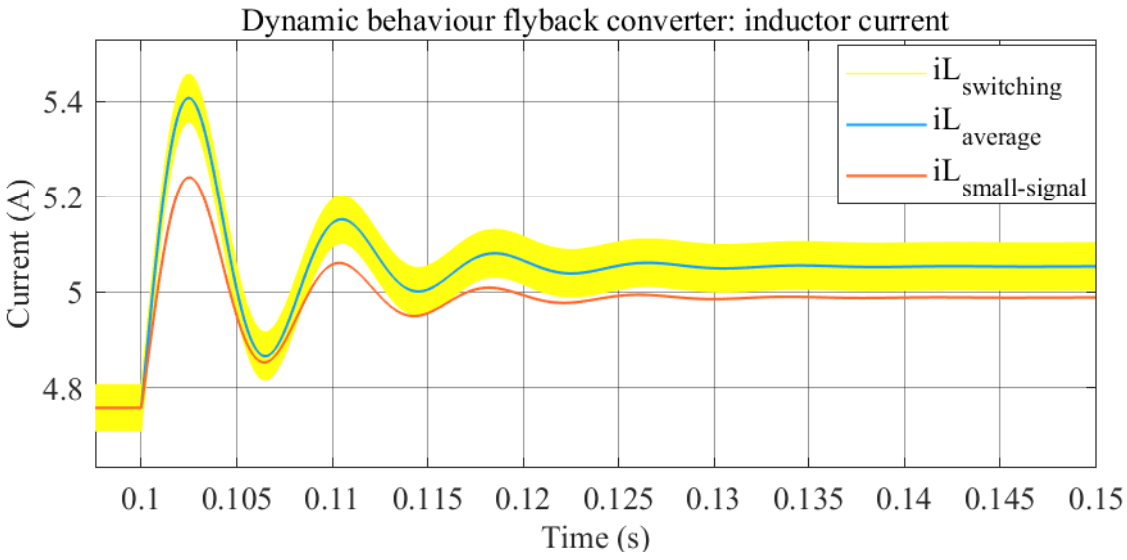

Figure 4-8: Time response to a small change of the duty cycle of the flyback converter: battery voltage.

where a constant voltage with cut-off value is applied and maintained until the current decreases to zero value and the battery reaches full charge. This charging strategy is shown in Figure 4-9.

To avoid that small variations of the voltage constantly change from current control to voltage control and vice-versa, there is a hysteresis algorithm implemented.

The key to the hysteresis control is that when the current control is active and the voltage reaches the cut-off value, it does not change to voltage control until it reaches a safety margin. Same thing happens when the voltage decreases below the cut-off voltage, there is a margin to delay the change to current control. Figure 4-9 shows the CC-CV control strategy with and without hysteresis.

There are a few limitations that need to be taken into account. First, maximum and minimum voltage values of the battery must be known. While working is discharge mode, the battery should never go below the minimum level to avoid cell death. Second, the charging current should not go above the values given by the manufacturer of the selected battery to avoid any issues, like high temperatures that will compromise the battery.

Following this line of thinking, to preserve the battery life, the control algorithm

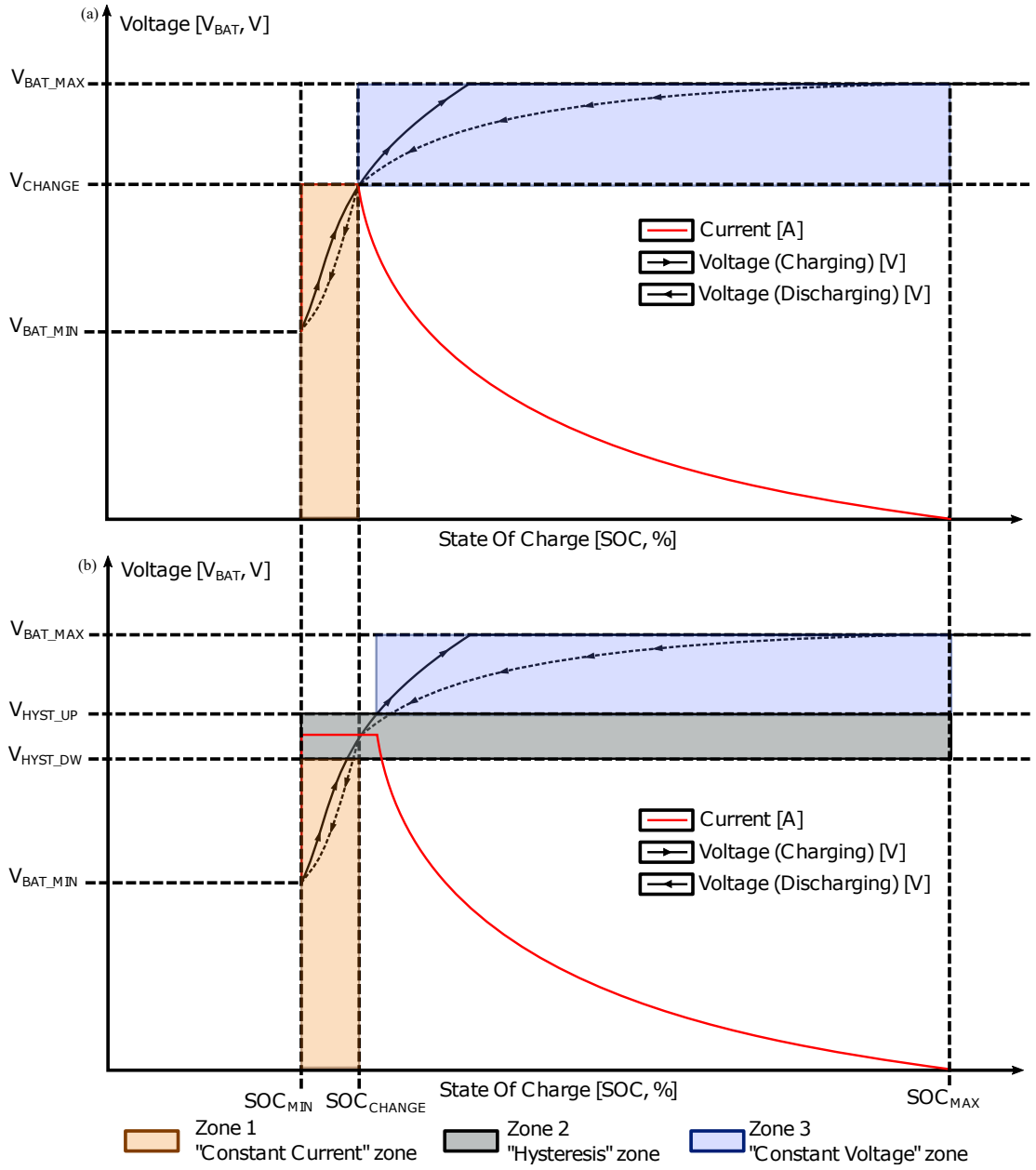

Figure 4-9: Battery charging scheme, with (a) and without (b) an hysteresis band between the constant current and the constant voltage charging modes.

takes into account the State of Charge (SoC). By manufacturer's recommendation, battery charge should stay between 25% and 75% to extend the total number of life cycles [29].

The proposed state machine flow diagram is shown in Figure 4-10. For the V2G utilization, the current control will be used by setting a negative current reference

that will reverse the power flow. However, it will only enter the discharge state if the battery SoC is between those levels.

In the charging process case, the SoC must be below that 75% to allow charging and will take into account the voltage level to move between the CC stage and the CV one.

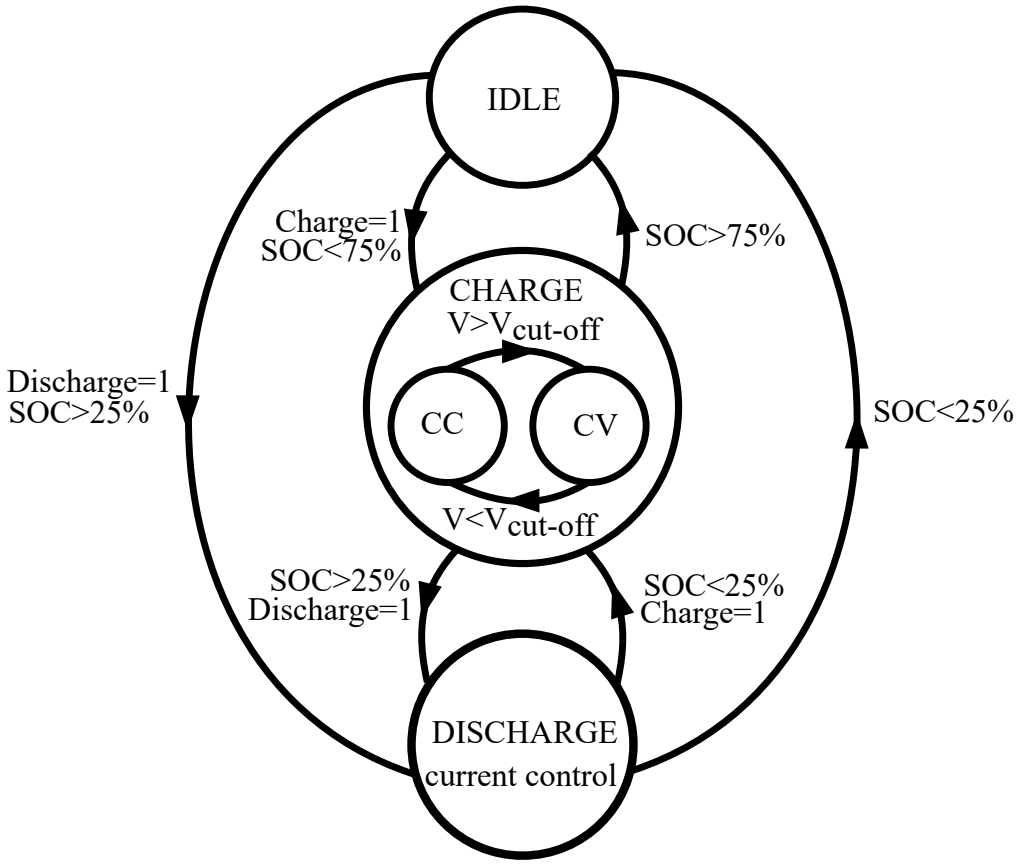

Figure 4-10: State machine flow diagram for switching between charge and discharge mode.

Moving on to the actual control strategy, as the dynamic behaviour of the flyback converter is much faster than the battery, it can be assumed that the transfer function of the converter is equal to 1. That leaves a cascade control that presumes the current control to be applied to the filter and the voltage control to the battery transfer function. Then, the proposed control scheme is shown in Figure 4-11, where d is the duty cycle calculated in each iteration.

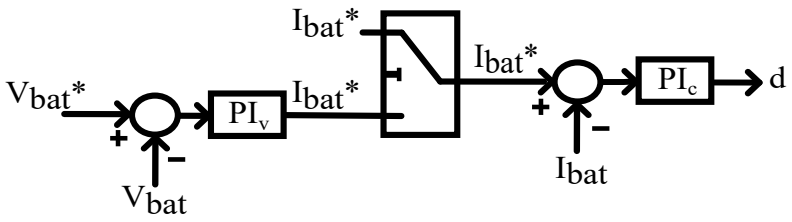

Figure 4-11: Control scheme for constant current-constant voltage control.

The closed loop control architecture is shown in Figure 4-12. As can be seen, the flyback converter plant is considered to be ≈1, the duty acts on the converter and control the the output voltage. As it is a closed loop with the filter and battery, by controlling the voltage and current flowing through the filter, it indirectly controls the flyback converter duty cycle to increase or decrease the output voltage as needed.

With this control structure in mind, it can be assumed that, as long as the DC-DC converter keeps being fast enough that the plant can be considered to be = 1 in comparison to the battery, any topology could be used instead of the flyback converter. That is because the control strategy is actually based on controlling the filter current and voltage, not the converter.

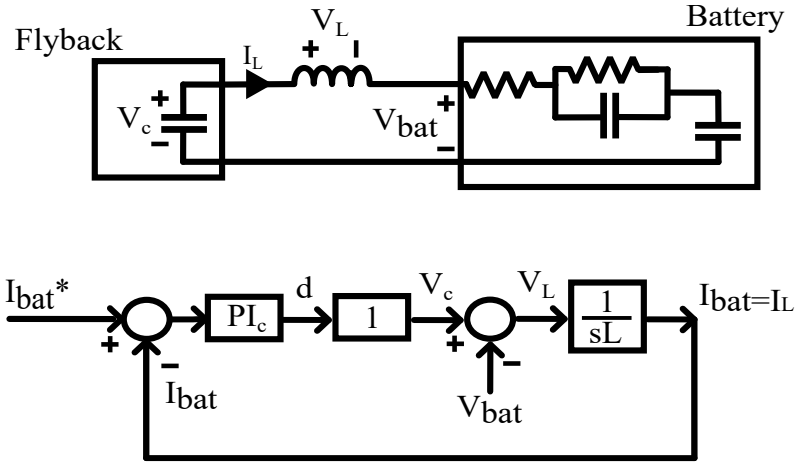

Figure 4-12: Closed loop control scheme for current control.

As can also be seen the first order approximation of the battery, that will be now explained in more detail.

4.5.1 Battery modelling

In order to know the battery transfer function, the dynamic behaviour of the battery must be analyzed.

In this thesis, the battery transfer function is modelled as a first order system based on the data given by the manufacturer of the selected battery. A more detailed explanation of this process can be found in Appendix D.

The selected battery in this thesis is the Bosch PowerPack 300 [26]. The values for the first order battery model are compiled at Table 4.3.

Parameter	Data	Value	Units
Series resistance	R_s	42.5	mΩ
Dynamic resitance	R_{dyn}	90	mΩ
Dynamic capacitor	C_{dyn}	12	F
Open-circuit capacitor	C_{soc}	2500	F

Table 4.3: Value of the battery model parameters.

As the open circuit capacitor C_{soc} of the battery is so large, it can be considered as a voltage source. Therefore, the transfer function of the battery is assumed to be based on a first order RC circuit. The proposed equivalent model for the battery is shown in Figure 4-13.

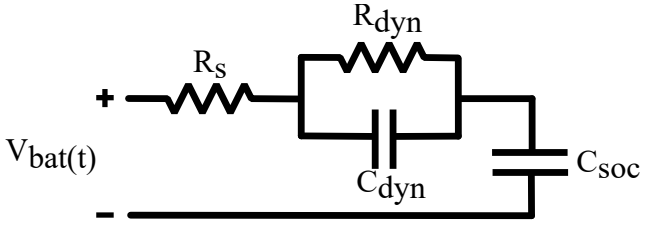

Figure 4-13: First order battery model.

4.5.2 Tunning of the controllers

Given those two assumptions, the tunning of both PI regulators can be obtained by pole-cancellation method, which leads to equations from (4.13) to (4.16) considering the PI controllers are in ideal form. Where the bandwidth for the current control

should be at least 10 times faster than the voltage control (as usual for cascade control architectures).

Also, the response produced by the PI controllers must not have any overshoot, which will match the really slow dynamic response inherited to the battery.

$$kp_c = 2\pi BW_c L_f \tag{4.13}$$

$$Ti_c = L_f / R_f \tag{4.14}$$

$$kp_v = 2\pi BW_v C_{dyn} \tag{4.15}$$

$$Ti_v = R_{dyn} C_{dyn} \tag{4.16}$$

Lastly, to avoid accumulation of control action of the voltage control when it is not active, there is an algorithm implemented that makes the input to the PI_v (error signal of the voltage reference) equal to zero when there is no voltage control. In reality, this means that the control action is disabled whenever the voltage control is disabled.

In the case of the flyback converter, the following values for the PI regulators shown in Table 4.4 are obtained. As the parasitic resistance value of the filter is not known but taken into account in the tunning equations, the time constant for the current PI controller is almost arbitrary depending on the desired behaviour.

Data	Value	Data	Value
BW_c	20 Hz	BW_v	0.02 Hz
Kp_c	0.0118	Kp_v	9.47
Ti_c	0.01	Ti_v	1

Table 4.4: Values of the PI controllers for the flyback converter.

The correct behaviour of the control strategy proposed in this Chapter will be tested and the results will be shown in Chapter 5.

Chapter 5

Simulations and Results

In this chapter, the simulations performed in this thesis will be explained in order to test the correct behaviour of the charger.

Two important things to take into account in the simulations performed in this thesis is that both converters are tested with the average model. As explained, this provides faster simulations and, therefore, less computational time. However, switching behaviour will not be shown in the results. Also, in all simulations the first order battery model is implemented, except the specified ones.

In the following sections, the simulations performed on the single-phase rectifier will be explained and results will be studied. Then, the flyback converter will also be tested, as well as the control algorithm explained in previous chapters based on the SoC of the battery.

Lastly, the entire system will be tested and proven to be stable enough to support the charge and discharge of the selected battery or a power rated similar one.

5.1 Single-Phase rectifier with Power Factor correction

In previous chapters of this thesis it was already stated that the DC-link voltage and current control followed the reference in the desired way. Now, a few additional

features of this topology can be tested.

The first thing that is going to be shown is the ability of the single-phase converter to change power levels and the direction of the power flow while maintaining a stable DC-link voltage.

By changing the $R_{load}$the demanded power changes. In this test, the power was changed with a step from 200 W to 500 W and then another step from 200 W to 700 W. In Figure 5-1 it can be seen that the DC-link voltage goes back to the steady-state value in 0.1 seconds approximately. It can also be seen that the power is high enough to support at least 3 flyback converters connected to the DC-link side.

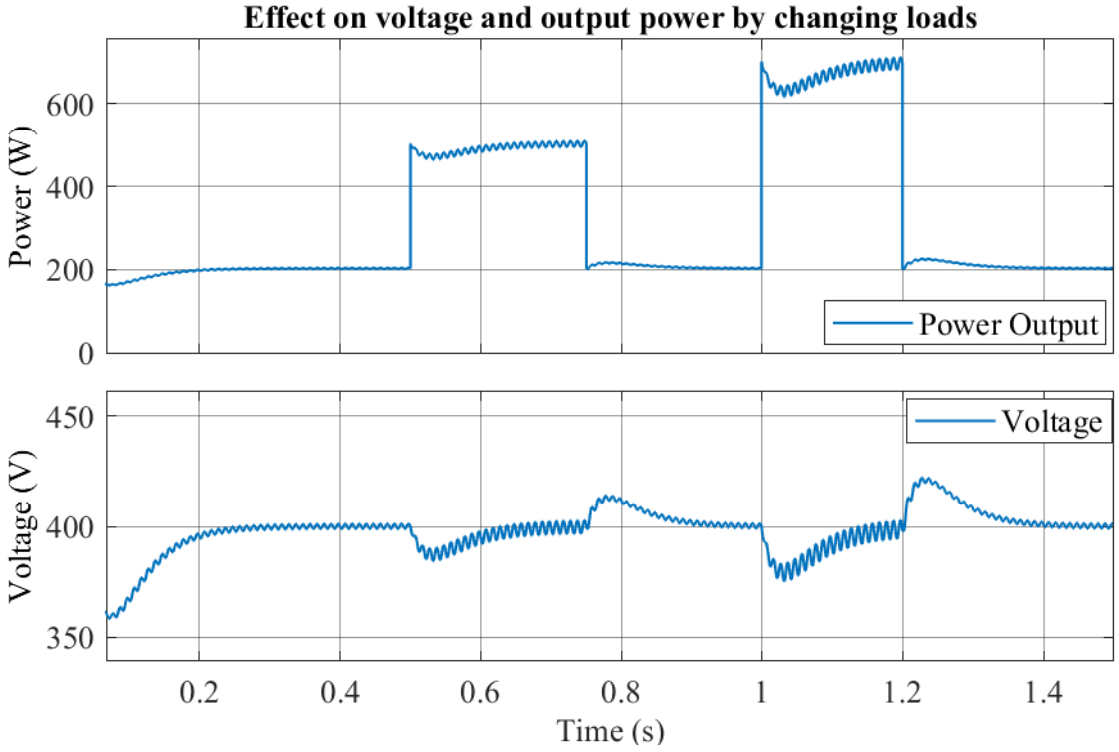

Figure 5-1: Effect on the DC-link voltage and output power by changing the load.

Now, by introducing a current from the load, the power flow changes directions and the converter feeds current to the grid. The behaviour in this case is shown in Figure 5-2. As can be seen, even injecting a sudden current to change the direction of the power flow, the DC-link voltage goes back to the desired value in less than 1 second.

Last important thing to show is the power factor correction. In figure 5-3, the grid

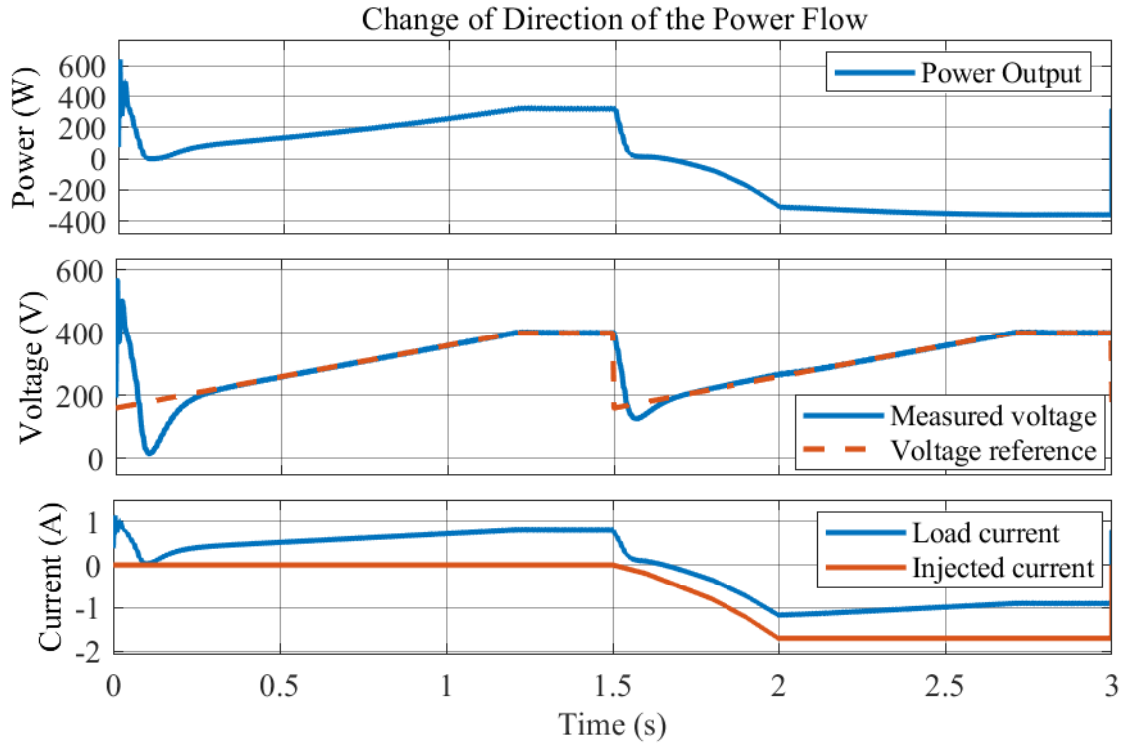

Figure 5-2: Effect on the DC-link voltage and output power by changing the power flow.

voltage and the grid current are in phase. That makes the Power Factor equal to unity, as designed. Note that the grid voltage has been divided by 30 for representation clarity purposes.

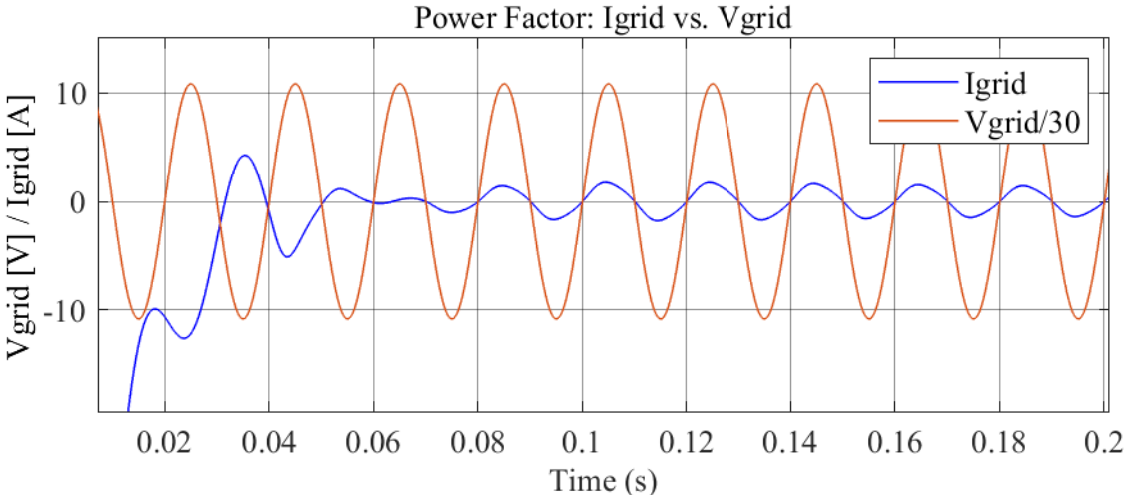

Figure 5-3: Power factor: i_{grid} vs v_{grid}.

5.2 Flyback converter

Moving on to the flyback converter, the Simulink's simulation is composed by the average model and the control strategy explained in Chapter 4. Introducing the aforementioned data into the Simulink's simulation, the following results are obtained.

First, the control strategy CC-CV is shown in Figure 5-4. In this figure are represented the two different stages of this kind of control. First, the constant current control is shown from the start to 5.5 seconds approximately. Then, the battery voltage reaches the cut-off value and it goes to the constant voltage stage. That is shown from 5.5 seconds till the end.

As can be seen, at first the battery current takes about 5 seconds to reach the reference current value. However, after that settling time, it follows the reference exactly.

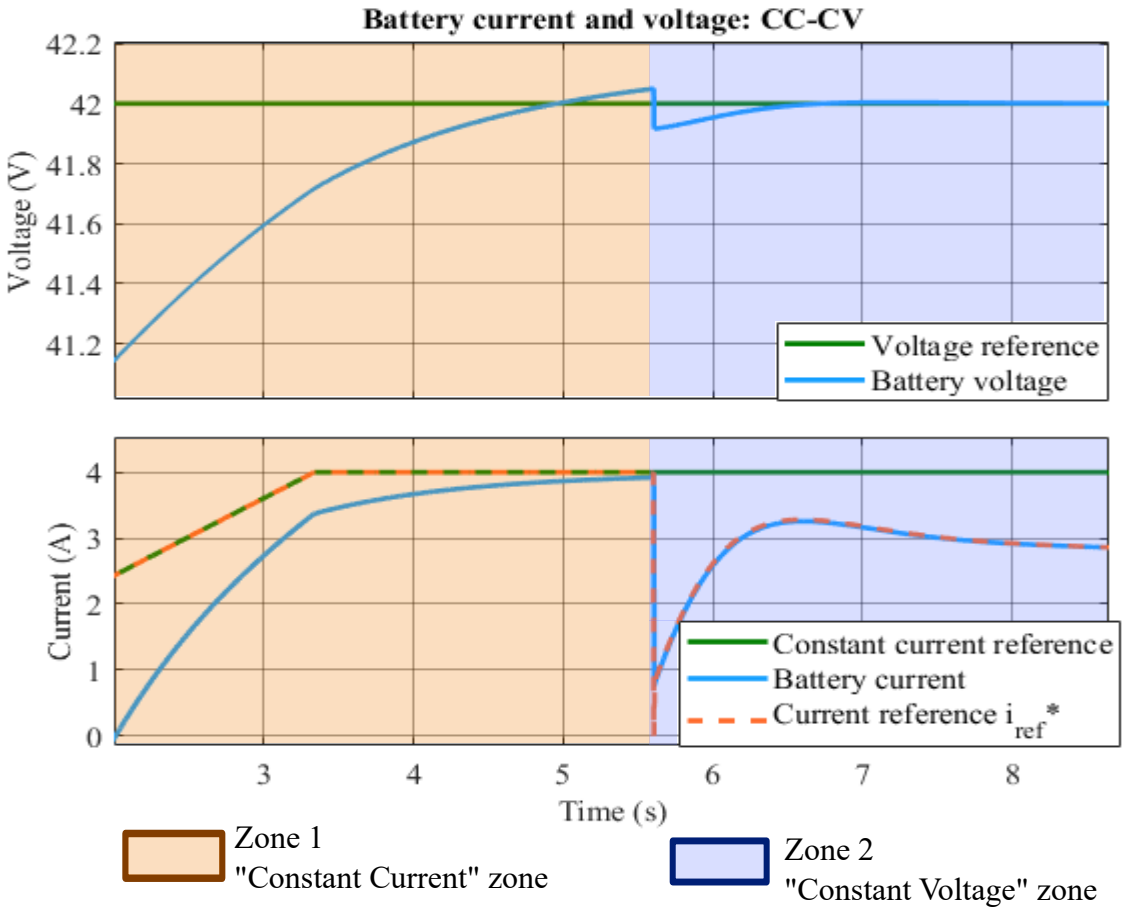

Figure 5-4: Battery current and voltage: change between CC - CV.

The change between the charge and discharge mode is also proven in Figure 5-5. From the start to 8.5 seconds the power is flowing to the battery. From there, the battery is injecting power to the grid and it can be seen that the battery voltage decreases. In Figure 5-5 it is represented the change between the charge in constant current stage to discharge mode.

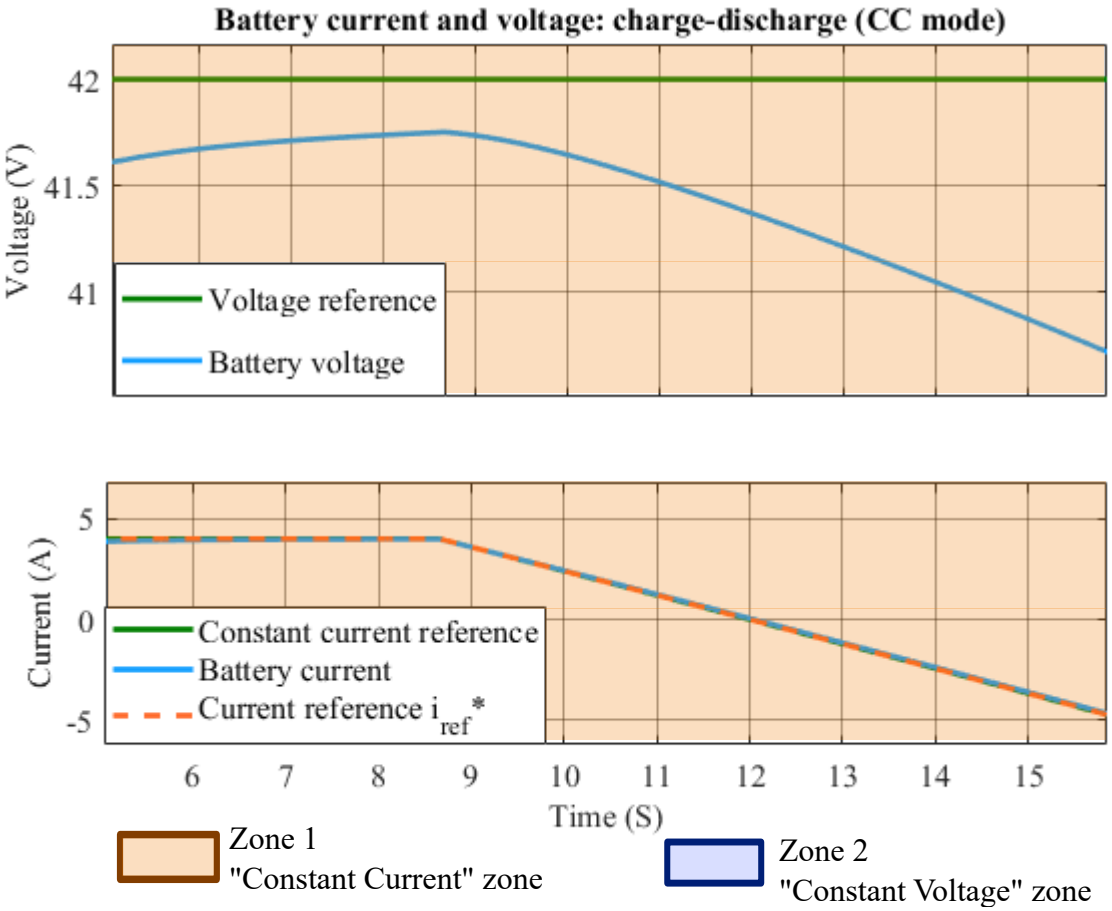

Figure 5-5: Battery current and voltage: change between charge and discharge from CC mode.

There is also another possibility, the change between the constant voltage stage to discharge. This case is represented in Figure 5-6. In this stage, the current is already close to zero. To prevent the battery current to go up in a high peak, it does not follow the current reference until it reaches zero value, and then decreases with it.

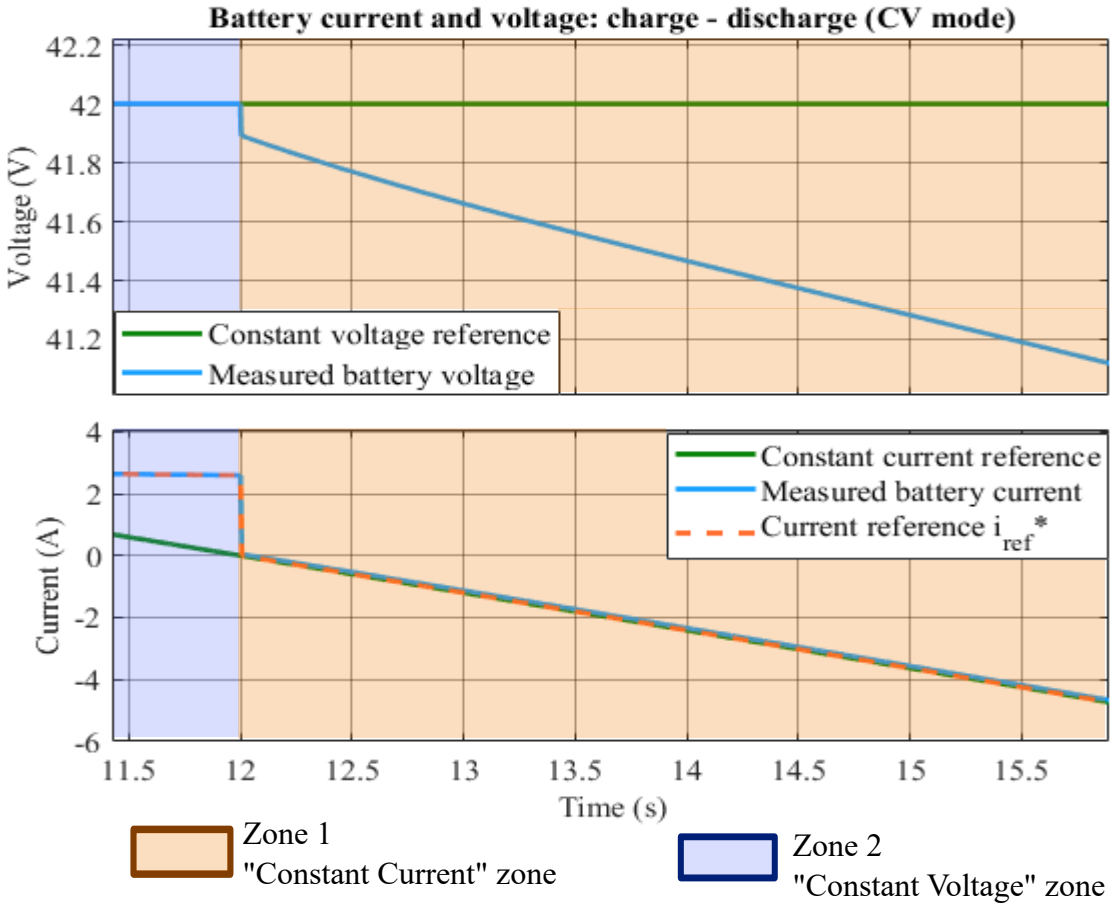

Figure 5-6: Battery current and voltage: change between charge and discharge from CV mode.

Finally, another situation was considered. As the first order model of the battery was obtained by theoretical values, there is a high chance that the physical battery has different values than the ones obtained. Also, in the case of a change in the battery, it is very likely that the values obtained in this thesis are not exact. Because of that, the control strategy has to work even if the calculated value of the $Cdyn$ is not the one used for the tunning of the PIs.

To test the correct behaviour of the control strategy, even if one of those scenarios

is given, the $Cdyn$ value, which represents the dynamic behaviour of the battery, is tested as half and twice the calculated value.

Figure 5-7 shows the behaviour for a battery with half the size of $Cdyn$. As can be seen, when switching to CV mode at 3.5 seconds, the battery current has a small error with respect to the reference. But after that it follows it with zero error.

Figure 5-8 shows the behaviour for a battery twice the size of $Cdyn$. In this case, the behaviour is the same that it has with the initial values.

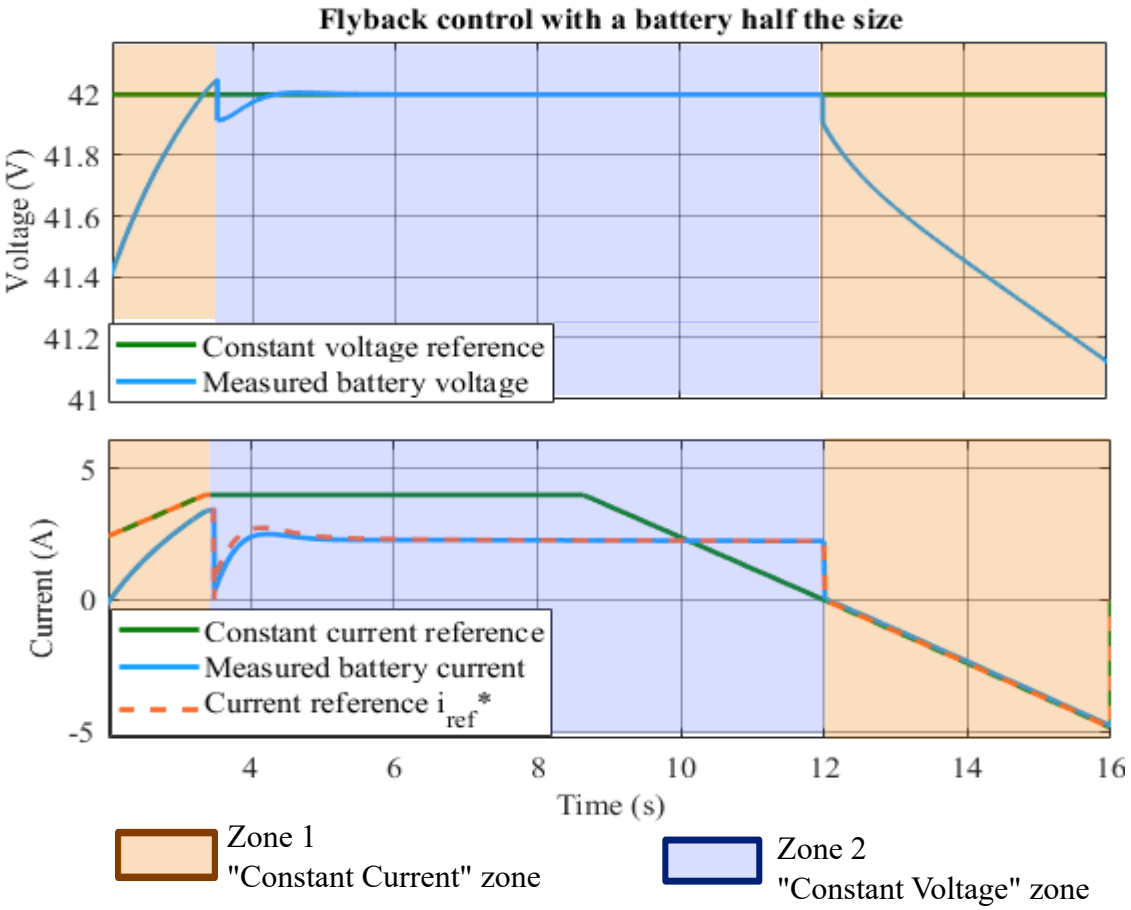

Figure 5-7: Flyback control with a battery half the capacity.

5.3 Bidirectional EV charger

In this section, the two converters are unified. The main goal in this section is to show that the behaviour of each converter does not really affect the other one.

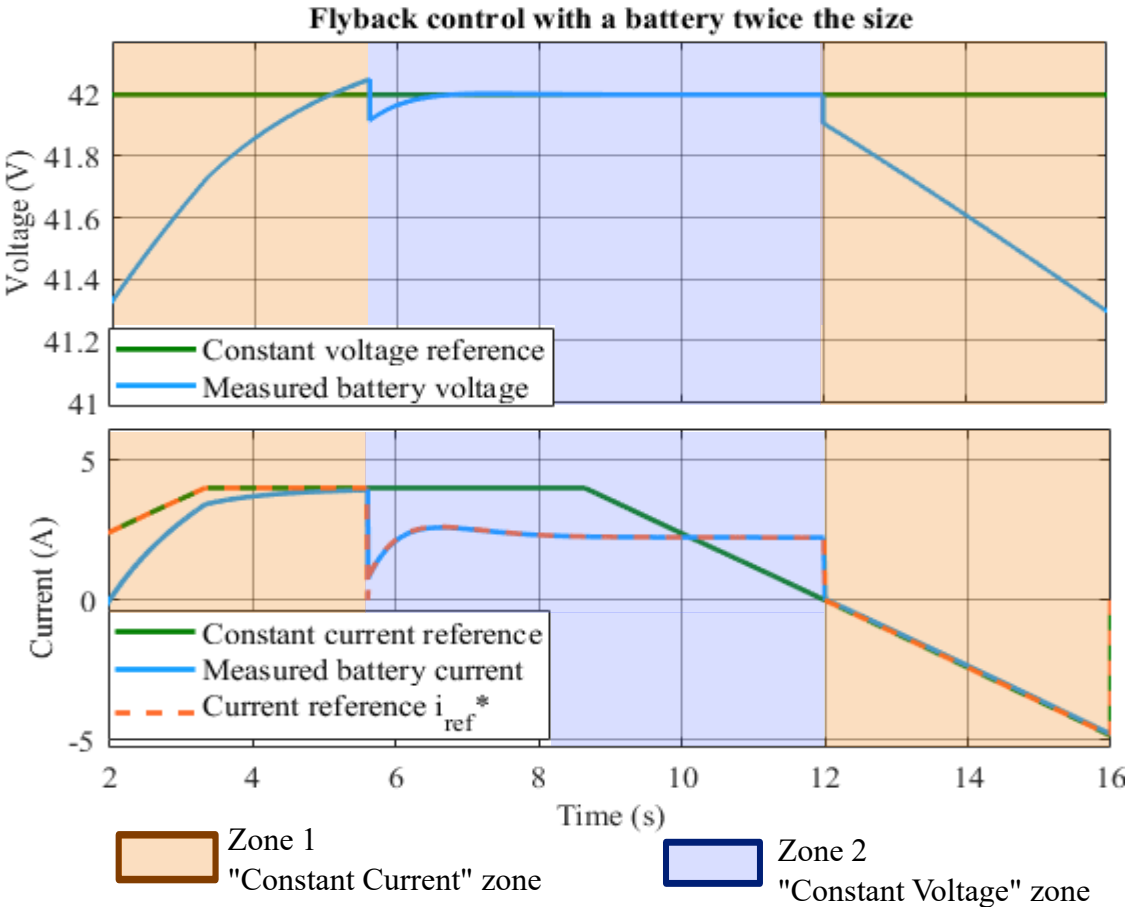

Figure 5-8: Flyback control with a battery twice the capacity.

To prove this stability, Figure 5-9 shows the DC-link voltage through the different changes represented in Figure 5-10. That includes the change between CC mode to CV mode at 5 seconds, and the change between charge and discharge at 12 seconds.

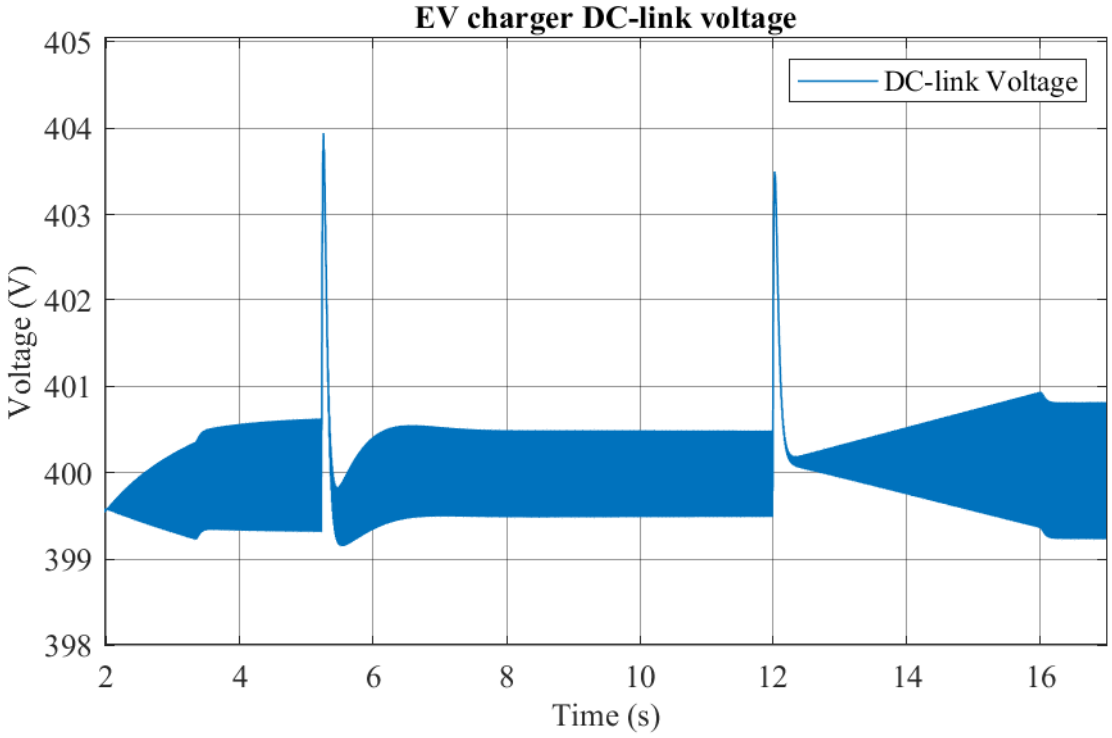

Figure 5-9: EV charger: DC-link voltage.

Lastly, to check the correct behaviour of the charge-discharge control algorithm that protects the battery, a simulation test was performed. To do this test, the first order battery model was substituted with the Simulink battery model as one of its measurements port is the SoC of the battery. The lower and upper limits in this thesis are set to 25% and 75%, respectively.

As shown in Figure 5-11, the EV charger stops the discharge when it reaches the lower limit of the SoC. In Figure 5-12, when the battery reaches the upper limit value, the algorithm stops the charge.

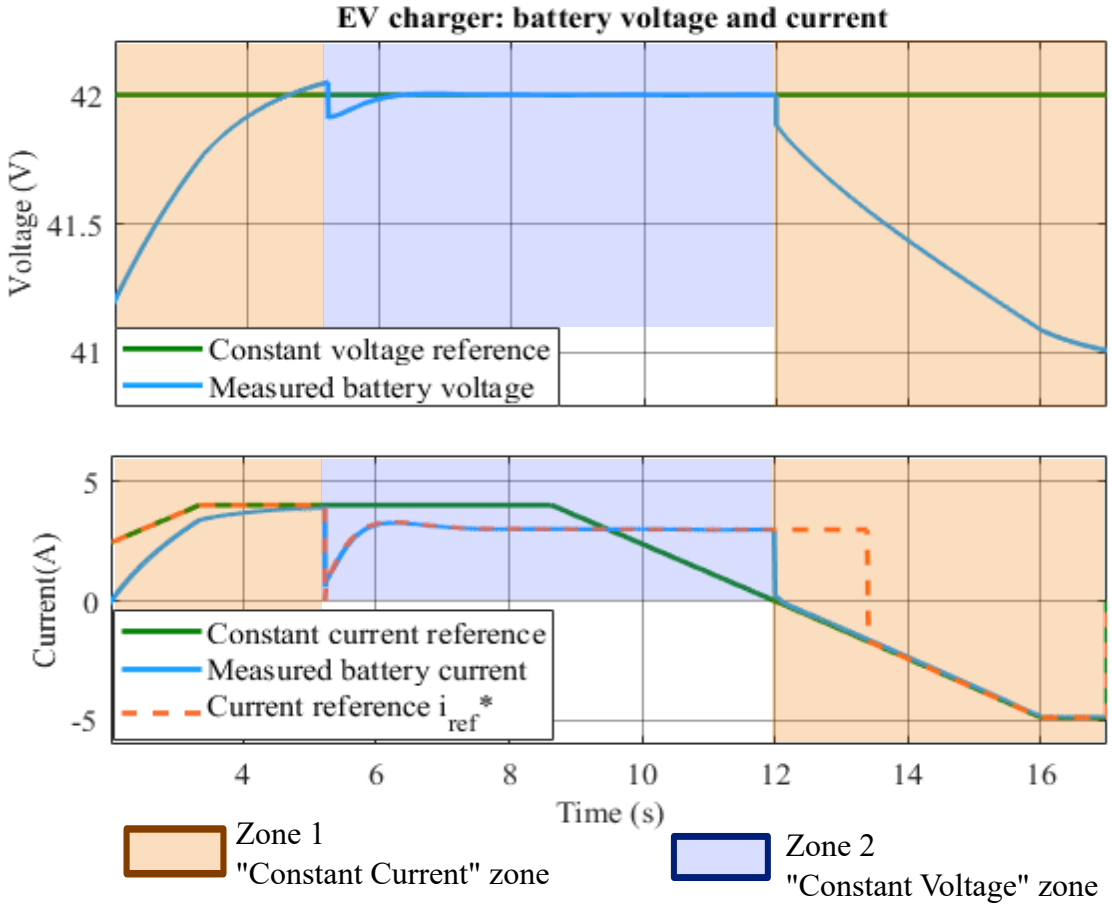

Figure 5-10: EV charger: Battery current and voltage: charge(CC-CV)-discharge.

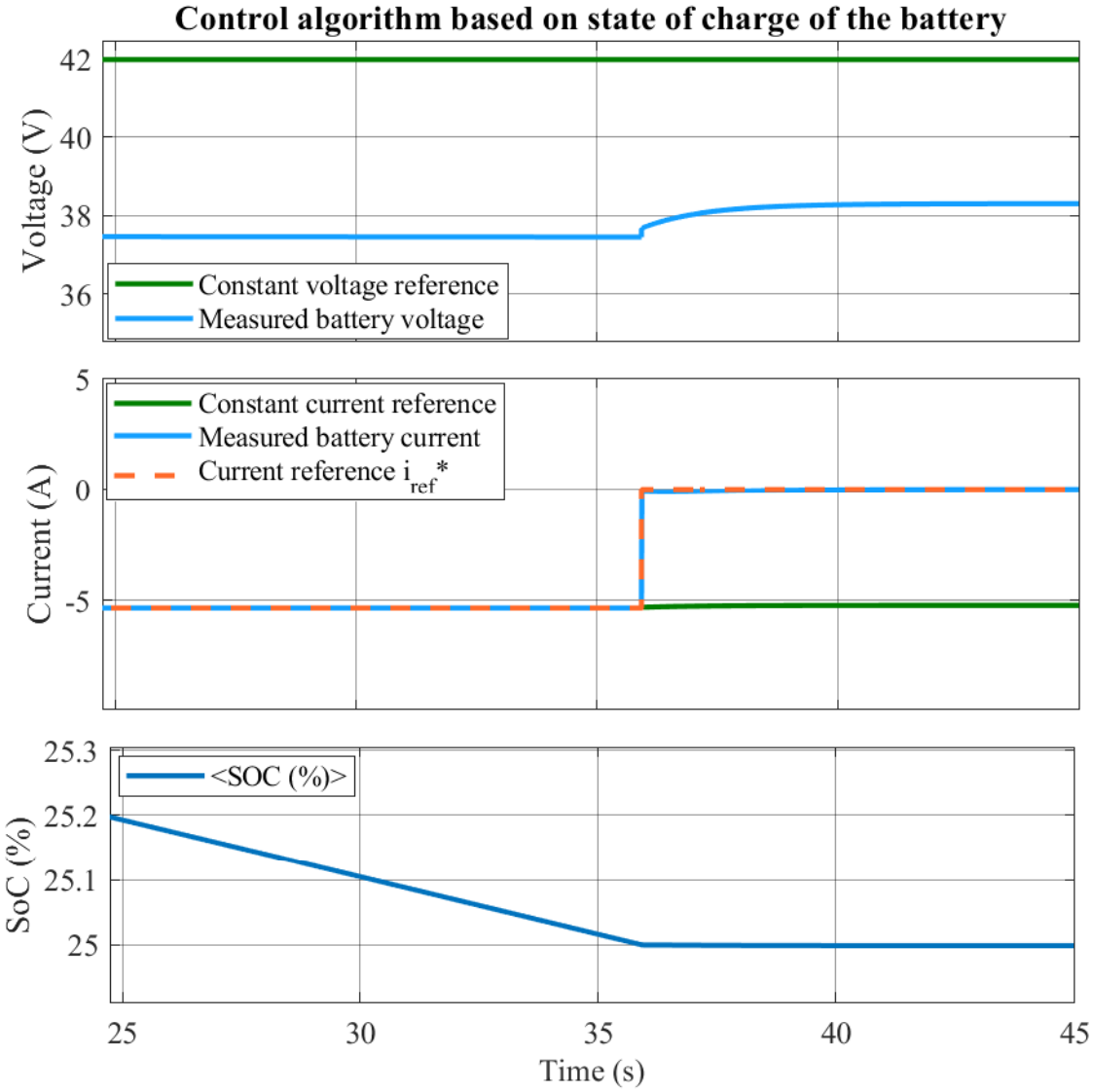

Figure 5-11: Discharging stop at 25 % SoC.

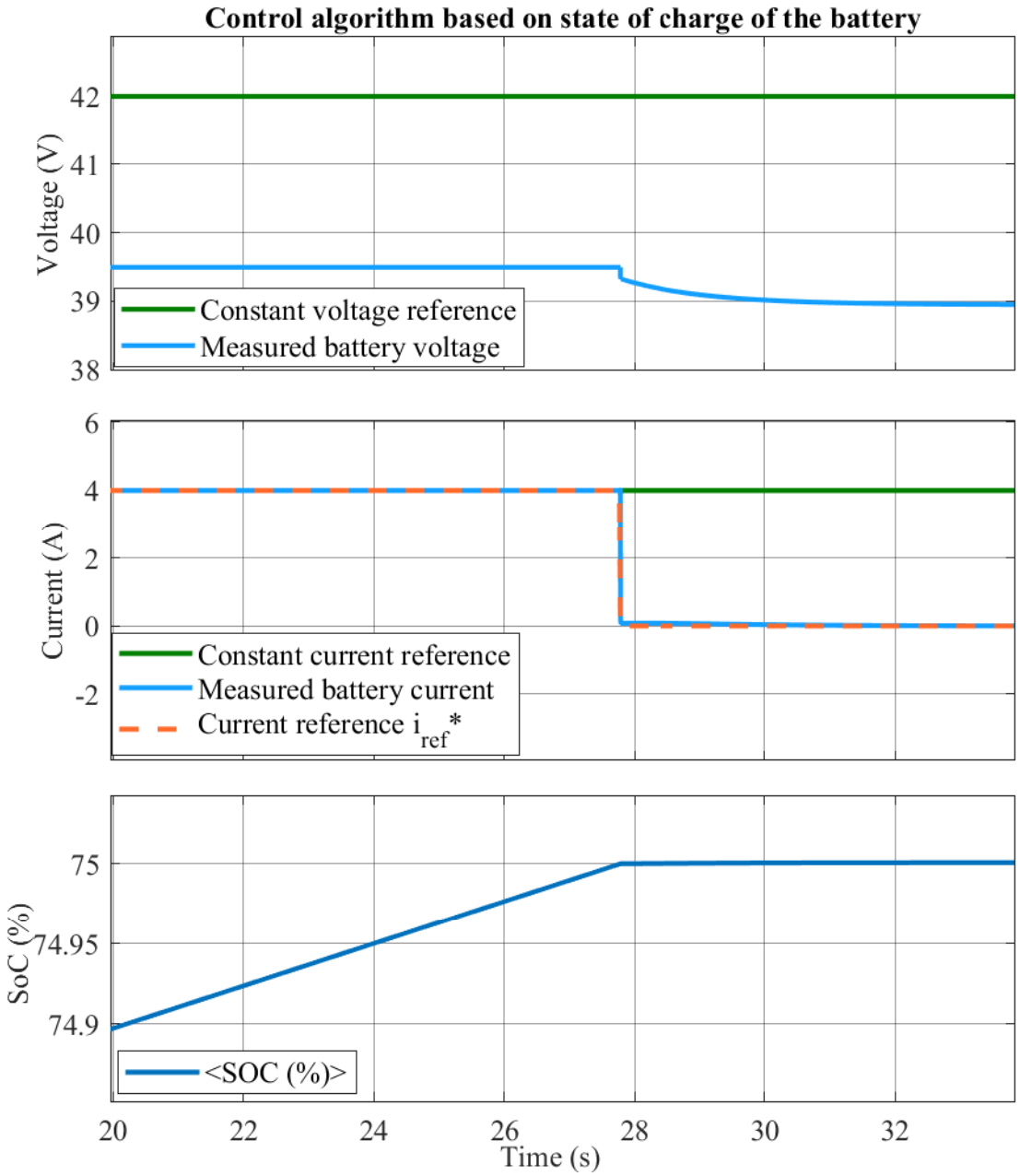

Figure 5-12: Charging stop at 75 % SoC.

Chapter 6

Conclusions and Future Work

In this chapter, the most important points will be established and summarized in the Conclusions section. Then, a few improvements and proposed future work will also be mentioned.

6.1 Conclusions

To summarize the results of the simulations shown in the previous section, a few important points can be highlighted.

Starting by the mathematical models that were studied and tested in this thesis, it can be proven that the average model of both the full-bridge and the flyback converter behave the same as the switching model. Also, the small-signal model of the flyback converter was studied and proven dynamically correct.

The first order equivalent model of the battery was also obtained and proven to have the same dynamic behaviour as the Simulink battery model based on data from the selected manufacturer.

Now, regarding the general behaviour of the system, it works as designed as a battery charger and also injecting power to the grid following a power command. This means that the initial purposes of this project are met. The designed control strategy is validated for both the AC-DC and DC-DC converter.

Focusing on the details, the assumptions made to design the control strategy seem

to be accurate and not really affect the behaviour of the system. As, for example, the flyback converter is assumed to have a plant ≈ 1, as long as this condition is met, any other topology could substitute the flyback converter.

Another thing to take into account is that the power factor has been achieved to be equal to 1 at all times. This means that this system will not affect the reactive power of the grid. However, it will have some effects since other kind of issues, like harmonics, are not taken into account in this thesis.

Moreover, the DC-link is strong enough to maintain the reference level even with significant changes in the power flow. So it can be assumed to be also strong enough to support more than one connected converter.

Last thing to consider is the difference of switching frequency between the two converters. This is not a cause for issues as they are different stages, the AC-DC is proposed to be off-board and the DC-DC converter is on-board and there could be multiple converters connected to the DC-link. Therefore, there is no benefit in working at the same frequency with both converters at this point, and the component requirements could be more difficult in that case.

6.2 Future work

There are a few things that could be improved in this thesis. First, as explained, the AC-DC converter and the DC-DC converter are not working at the same switching frequency. This might not cause an issue in simulations, but it could create resonance problems in the physical model. It is less likely as both converters are not physically closed by implementing the off-board and on-board design, but it is definitely an issue to consider.

The use of different kind of switching devices such as silicon carbide (SiC) technology or GAN Transistors could potentially lead to better behaviour. The switching behaviour and losses would have to be studied.

In the same area, taking into account efficiency and switching losses could be another improvement, as minimizing losses strategies were not contemplated in this

thesis.

Next, the implementation of the control algorithm would be easier and more efficient if performed by a C language code that could be exported to a micro-controller. It would also improve battery charging security, as it could also take into account the temperature of the battery to prevent damage.

Another thing to consider is that the flyback converter topology was selected due to its cost and simplicity. However, it is not the most effective topology and, considering a EV battery, it is not capable of providing enough power. Another topology might be considered such as DAB converter or, the most common one nowadays, a resonant converter.

Lastly, regarding the purpose of this thesis, it was explained in the Introduction that this kind of load could be used to stabilized or correct active power in the grid. However, in this thesis the only scenario is a power factor equal to one. Another power factor correction strategy could be proposed to avoid the negative effects of this kind of load.

Appendix A

Single-Phase rectifier: average model

As explained in Section 3, to study the dynamic behaviour of the Single-Phase rectifier is easier to test it as an inverter. The proposed topology is shown in Figure A-1.

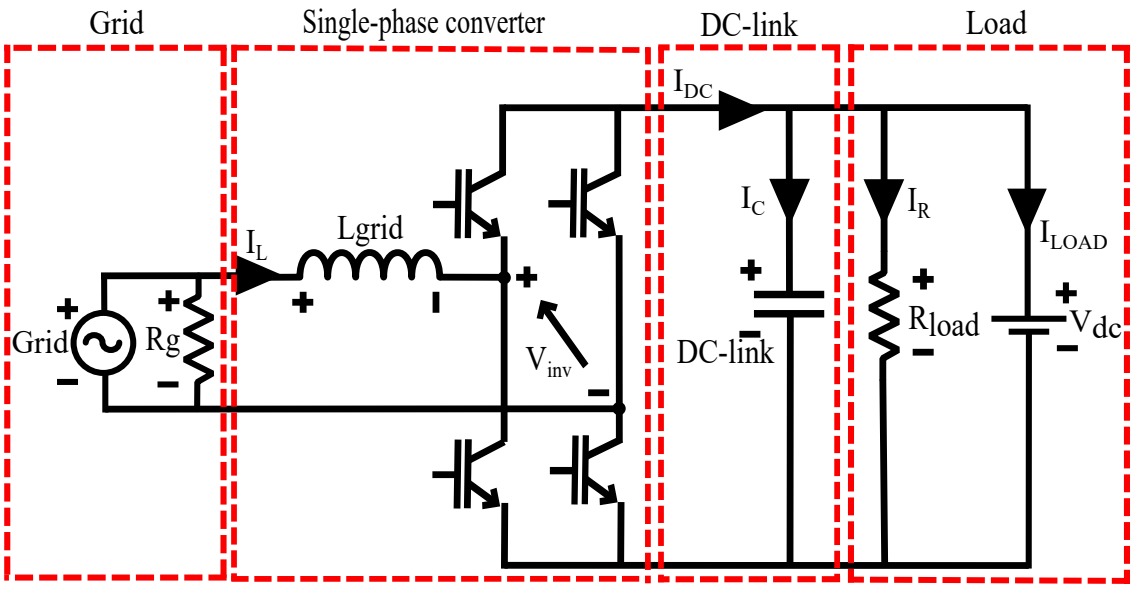

Figure A-1: Single-Phase inverter

To extract the relationships, the circuit has to be studied in intervals. First, the time interval (d) happens when Q1 and Q4 are on is shown in Figure A-2. From this

case, relationships (A.1) and (A.2) are known.

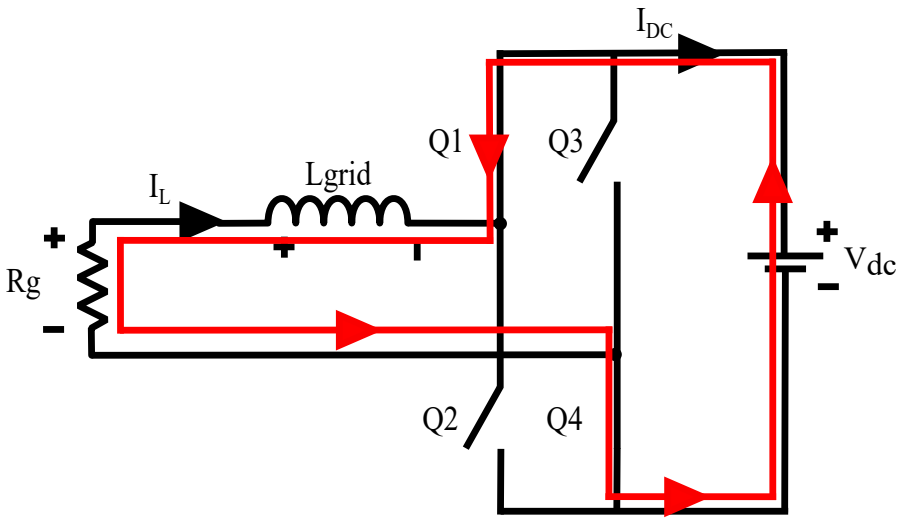

Figure A-2: Single-Phase inverter when Q1 and Q4 are ON

$$-V_{inv}(t) + V_{DC}(t) = 0 \tag{A.1}$$

$$i_{DC}(t) = i_L(t) \tag{A.2}$$

From the second time interval (1-d), the Q2 and Q3 switches are on. This situation is shown in Figure A-3, and the relationships (A.3) and (A.4) are extracted.

$$-V_{inv}(t) - V_{DC}(t) = 0 \tag{A.3}$$

$$i_{DC}(t) = -i_L(t) \tag{A.4}$$

The next step is to combine both intervals d(t) and d'(t) to average the equations over one switching period. The averaged equations are shown in (A.5) and (A.6), where $d' = 1 - d$.

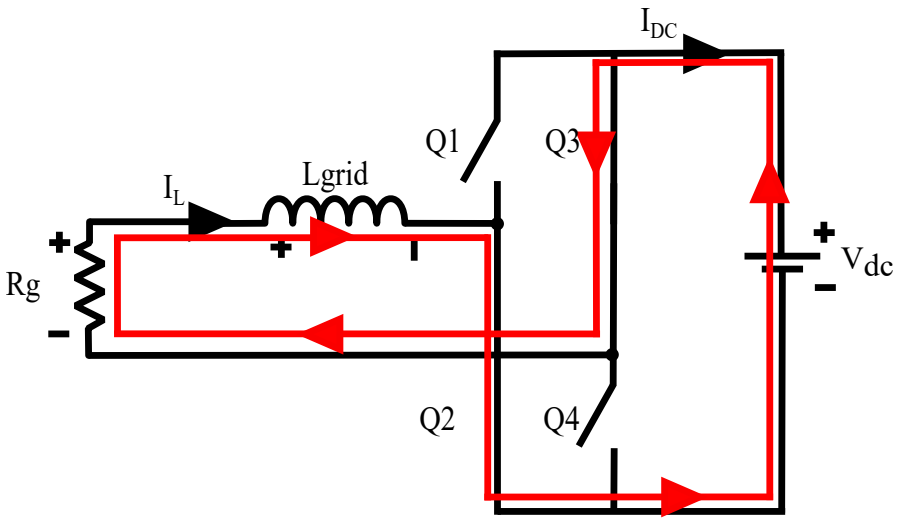

Figure A-3: Single-Phase inverter when Q2 and Q3 are ON

$$< V_{inv}(t) >= d(t)(V_{DC}(t)) + d'(t)(-V_{DC}(t)) \tag{A.5}$$

$$< i_{DC}(t) >= d(t)(i_L(t)) + d'(t)(-i_L(t)) \tag{A.6}$$

Now, to linearize those equations, all averaged signals can be expressed as a DC term plus a small AC variations by applying the relationships shown in (A.7) to (A.12).

$$d(t) = D + \widehat{d}(t) \tag{A.7}$$

$$d'(t) = D' - \widehat{d}(t) \tag{A.8}$$

$$V_{dc}(t) = V_{dc} + \widehat{v_{dc}}(t) \tag{A.9}$$

$$V_{inv}(t) = V_{inv} + \widehat{v_{inv}}(t) \tag{A.10}$$

$$I_{DC}(t) = I_{DC} + \widehat{i_{DC}}(t) \tag{A.11}$$

$$I_L(t) = I_L + \widehat{i_L}(t) \tag{A.12}$$

The resulting linearized equations are shown in (A.13) and (A.14) [30],

$$L\frac{d<(I_L+\widehat{i_L}(t))>}{dt} = (D+\widehat{d}(t))(V_{DC}+\widehat{v_{DC}}(t)) - (V_{inv}+\widehat{v_{inv}}(t)) + (D'-\widehat{d}(t))(-V_{DC}-\widehat{v_{DC}}(t)) \tag{A.13}$$

$$<(I_{DC}+\widehat{i_{DC}}(t))>=(D+\widehat{d}(t))((I_L+\widehat{i_L}(t)))+(D'-\widehat{d}(t))(-I_L-\widehat{i_L}(t)) \tag{A.14}$$

By multiplying and collecting terms, (A.15) and (A.16) are obtained. These equations contains three types of terms. The DC terms contain no time-varying quantities and will be used to implement the average model.

$$\begin{aligned} L\ \frac{d(I_L+\widehat{i_L}(t))}{dt} = & \underbrace{-V_{inv}+DV_{DC}-D'V_{DC}}_{DC\ terms} \\ & - \underbrace{\widehat{v_{inv}}(t)+D\widehat{v_{DC}}(t)+\widehat{d}(t)V_{DC}-D'\widehat{v_{DC}}(t)+\widehat{d}(t)V_{DC}}_{1^{st}\ order\ AC\ terms} \\ & + \underbrace{\widehat{d}(t)\cdot\widehat{v_{dc}}(t)+\widehat{d}(t)\cdot\widehat{v_{dc}}(t)}_{2^{nd}\ order\ AC\ terms} \end{aligned} \tag{A.15}$$

$$\begin{aligned} I_{DC}+\widehat{i_{DC}}(t) = & \underbrace{DI_L-D'I_L}_{DC\ terms} \\ & + \underbrace{D\widehat{i_L}(t)+\widehat{d}(t)I_L-D'\widehat{i_L}(t)-\widehat{d}(t)I_L}_{1^{st}\ order\ AC\ terms} \\ & + \underbrace{\widehat{d}(t)\widehat{i_L}(t)-\widehat{d}(t)(\widehat{-i_L}(t))}_{2^{nd}\ order\ AC\ terms} \end{aligned} \tag{A.16}$$

Which would leave the average model equations as shown in (A.17) and (A.18).

$$V_{inv} = (2D - 1)V_{DC} \tag{A.17}$$

$$I_{DC} = (2D - 1)I_L \tag{A.18}$$

Appendix B

Flyback converter: component design

As explained in Chapter 4, the same procedure is followed to calculate the minimum requirements for both charge and discharge mode (section 4.2). In this Appendix, first, the relationships that are the same between the two modes will be obtained, then they will be applied to calculate the turns ratio and the minimum value for the magnetizing inductance.

Lastly, the filter capacitance for the voltage ripple at the battery side will also be obtained. This entire calculation process is shown in more detail in [25].

Starting by analyzing the boundary between CCM and DCM, the current waveform of the magnetizing inductance is obtained and shown in Figure B-1, and it can be described by (B.1).

$$\Delta i_{Lm_{max}} = \frac{n \cdot V_{out} \cdot (1 - D_{min})}{f_s \cdot L_{m_{min}}} \tag{B.1}$$

The energy transferred from the input to the magnetizing inductance during one cycle is calculated as in (B.2).

$$W_{OB} = \frac{L_{m_{min}} \cdot \Delta i^2_{Lm_{max}}}{2} \tag{B.2}$$

Taking into account the DC output power, the relationship is shown in (B.3).

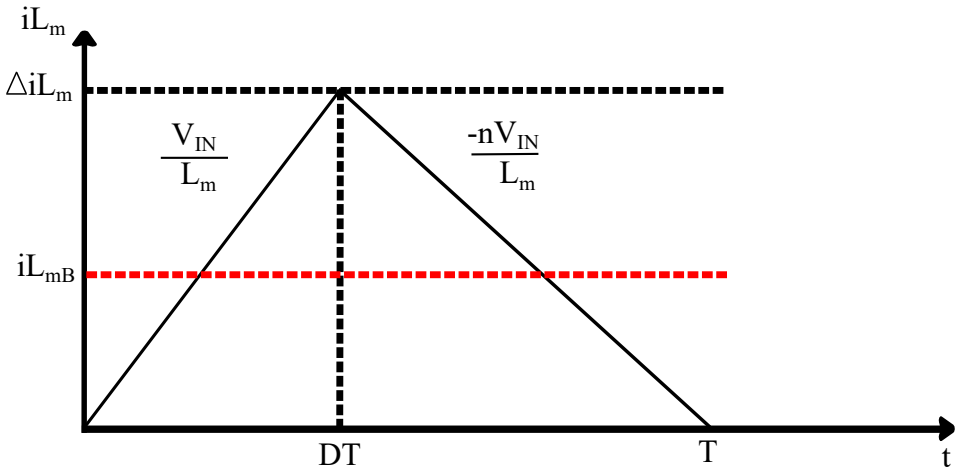

Figure B-1: Analysis of the boundary between CCM and DCM

$$P_{OB} = \frac{W_{OB}}{T} = f_s \cdot W_{OB} = \frac{f_s \cdot L_{m_{min}}}{2} \frac{n^2 \cdot V_{out}^2 \cdot (1 - D_{min})^2}{f_s^2 \cdot L_{m_{min}}^2} = \frac{n^2 \cdot V_{out}^2 \cdot (1 - D_{min})^2}{2 \cdot f_s \cdot L_{m_{min}}} \tag{B.3}$$

From that equation, the nonlinear relationship between the output power and the duty cycle is clear. As explained in [31], the evolution of the power with the duty is parabolic, as shown in Figure , which is the main reason why d_{max} is usually set at 0.4 or even 0.35. In this case, D_{max} will be set at 0.35.

Another initial value to consider is the efficiency of the converter, which, in the case of the flyback converter, is typically above 80 %. In this case, it will be taken into consideration the worst possible scenario and set $\eta = 80$ %.

B.1 Turns ratio n

1. Charging mode (G2V)

   Considering $V_{in} = 350$ - 400 V and $V_{out} = 42$ V and constant DC-link, the DC transfer function limits are set as shown in (B.4) and (B.5).

$$M_{VDC_{max}} = \frac{V_{out}}{V_{in_{max}}} = \frac{42}{400} = 0.120 \tag{B.4}$$

$$M_{VDC_{min}} = \frac{V_{out}}{V_{in_{min}}} = \frac{42}{350} = 0.105 \tag{B.5}$$

Now, for the turns ratio, the relationship is shown in (B.6).

$$n = \frac{D_{max}}{M_{VDC_{max}}(1 - D_{max})} \cdot \eta = \frac{0.35}{0.120 \times (1 - 0.35)} 0.8 = 3.59 \tag{B.6}$$

To round up, $n = 4$.

2. Discharging mode (V2G)

   Considering $V_{in} = 42$ V and $V_{out} = 400$ V, the DC transfer function is calculated as shown in equation (B.7).

$$M_{VDC_{max}} = \frac{V_{out}}{V_{in}} = \frac{400}{42} = 9.52 \tag{B.7}$$

Same as before, the turns ratio is calculated as shown in (B.8).

$$n = \frac{D_{max}}{M_{VDC_{max}}(1 - D_{max})} \cdot \eta = \frac{0.35}{9.52 \times (1 - 0.35)} 0.8 = 0.04 \tag{B.8}$$

As can be seen, the most restrictive one is the charge mode with a turns ratio $n = 4$.

B.2 Magnetizing inductance L_m

Considering that $f_s = 100kHz$:

1. Charging mode (G2V)

   In this mode, I_{out} = 0.10 - 4 A. The power limit values can be set as shown in (B.9) and (B.10), which are inside the usual power values of the flyback converter. The limit values for the R_{load} are calculated as shown in (B.11) and (B.12).

$$P_{out_{max}} = V_{out} \cdot I_{out_{max}} = 42 \times 4 = 168\ W \tag{B.9}$$

$$P_{out_{min}} = V_{out} \cdot I_{out_{min}} = 42 \times 0.10 = 4.2\ W \tag{B.10}$$

$$R_{l_{max}} = \frac{V_{out}}{I_{out_{max}}} = \frac{42}{4} = 420\ \Omega \tag{B.11}$$

$$R_{l_{min}} = \frac{V_{out}}{I_{out_{min}}} = \frac{42}{0.1} = 10.5\ \Omega \tag{B.12}$$

The minimum duty that will be used in this mode needs to be calculated.This relationship is shown in (B.13), as explained in Chapter 4.

$$D_{crit} = \frac{1}{\frac{V_{in}}{V_{out}}\frac{1}{n} + 1} = \frac{1}{\frac{400}{42}\frac{1}{4} + 1} = 0.2958 \tag{B.13}$$

Now, for the magnetizing inductance, the relationship is shown in (B.14).

$$L_{m_{min}} = \frac{n^2 \cdot R_{l_{max}} \cdot (1 - D_{crit})^2}{2 \cdot f_s} = \frac{4^2 \times 420 \times (1 - 0.2958)^2}{2 \times 100 \times 10^3} = 16.7\ mH \tag{B.14}$$

To round up, $L_{m_{min}} = 17mH$.

2. Discharging mode (V2G)

   In this case, the duty cycle will be set by the minimum voltage value that the battery can reach without suffering from cell degradation, and it is calculated as shown in (B.15).

$$D_{crit} = \frac{1}{\frac{V_{in}}{V_{out}}\frac{1}{n} + 1} = \frac{1}{\frac{400}{30}\frac{1}{4} + 1} = 0.2308 \tag{B.15}$$

Using that duty cycle to calculate the magnetizing inductance, the value of L_m in this case is shown in (B.16).

$$L_{m_{min}} = \frac{n^2 \cdot R_{l_{max}} \cdot (1 - D_{crit})^2}{2 \cdot f_s} = \frac{4^2 \times 420 \times (1 - 0.2308)^2}{2 \times 100 \times 10^3} = 19.9 \ mH \tag{B.16}$$

To round up, $L_{m_{min}} = 20mH$.

As can be seen, the minimum value for the magnetizing inductance is set by the discharge mode, and it is set at $L_m = 20mH$.

B.3 Stress in semi-conductors

With the magnetizing inductance value calculated previously, the peak-to-peak value of the AC current going through it can be obtained as shown in (B.17).

$$\Delta i_{L_{max}} = \frac{nV_o(1 - D_{crit})}{fsL_m} = \frac{4 \times 42 \times (1 - 0.2308)}{100 \times 10^3 \times 20 \times 10^{-3}} = 0.0646 \tag{B.17}$$

Now, for the DC current, it is taken into account that it happens when the voltage input is at the lowest, therefore, when $V_{in} = 350V$. Then, the maximum input current is calculated as shown in (B.18).

$$I_{in_{max}} = MV_{DC_{max}} I_{o_{max}} = 0.120 \times 4 = 0.48 \ A \tag{B.18}$$

Calculating stress in the semiconductors, for the primary side M1, the maximum current and voltages are calculated as shown in (B.19) and (B.20).

$$Is_{M1_{max}} = Iin_{max} + \frac{Iout_{max}}{n} + \frac{\Delta i_{L_{max}}}{2} = 0.48 + \frac{4}{4} + \frac{0.0646}{2} = 1.51 \ A \tag{B.19}$$

$$Vs_{M1_{max}} = V_{I_{max}} + nV_{out} = 400 + 4 \times 42 = 568 \ V \tag{B.20}$$

For the secondary-side MOSFET, M2, the relationships are shown in (B.21) and (B.22).

$$nIs_{M2_{max}} = Iin_{max} + Iout_{max} + \frac{n\Delta i_{L_{max}}}{2} = 4 \times 0.48 + 4 + \frac{4 \times 0.0646}{2} = 6.04 \tag{B.21}$$

$$Vs_{M2_{max}} = \frac{V_{I_{max}}}{n} + V_{out} = \frac{400}{4} + 42 = 142\ V \tag{B.22}$$

B.4 Filter capacitance C_{filter}

Considering now that the voltage ripple ratio is V_{ripple}/V_{out} $\leq$1%V, $V_{ripple} = 1\% \cdot 42 = 420mV$. Also, the peak-to-peak value of the voltage across the equivalent capacitor resistance $V_{rc_{pp}}$ is usually approximated as $< 10\%$ of the output voltage, therefore it is assumed to be $V_{rc_{pp}} = 350mV$.

The maximum rc, also called capacitor equivalent series resistance (esr), is calculated as follows in (B.23).

$$rc_{max} = \frac{V_{rc_{pp}}}{Is_{M2_{max}}} = \frac{350\ mV}{6.04\ A} = 57.94\ m\Omega \tag{B.23}$$

And considering the peak-to-peak voltage across the filter capacitance as $Vc_{pp} = 70mV$, the filter capacitance is calculated as shown in (B.24).

$$C_{min} = \frac{D_{max}V_{out}}{fsR_{L_{min}}Vc_{pp}} = 214.28\ \mu F \tag{B.24}$$

Therefore, a filter capacitor of 300 μF, 50 V and 300 $m\Omega$ is selected.

B.4.1 RL filter

Considering the current ripple $< 1\%$ and assuming that the internal resistance of the filter inductance is $R_f = 1.5m\Omega$:

$$L_f = \frac{(\Delta I_o)V_{bat}}{(\Delta I_o)I_o 2\pi f_s} = \frac{1\% \times 37.5}{1\% \times 4 \times 2\pi 100 \times 10^3} = 15\mu muH \tag{B.25}$$

Appendix C

Flyback converter: average & small-signal model

To start the analysis of this converter, there are a few assumptions to be made. Firstly, L_m is defined by the magnetizing inductance referred to the primary winding as depicted in Figure 4-1. Secondly, both MOSFET have an on resistance R_{on}. Thirdly, in order to simplify the equations, the equivalent battery model will be assumed to be a single resistor R_{bat}. Finally, other loss elements and switching losses are not considered in this case.

Now, to obtain the equivalent model, the first step is to analyze the converter by time sub-intervals. The first time interval is given when the MOSFET on the primary side, $Q1$, is ON (duty cycle D). This case is represented in Figure C-1, from where the inductor voltage $V_m(t)$, capacitor current $i_c(t)$ and converter input current $i_p(t)$ are defined as shown in (C.1), (C.2) and (C.3).

$$V_{dc}(t) = V_m(t) + V_{R_{on}}(t) \rightarrow V_m(t) = V_{dc}(t) - i_m(t) \cdot R_{on} \tag{C.1}$$

$$i_c(t) = -\frac{V_{bat}(t)}{R_{bat}} \tag{C.2}$$

$$i_p(t) = i_m(t) \tag{C.3}$$

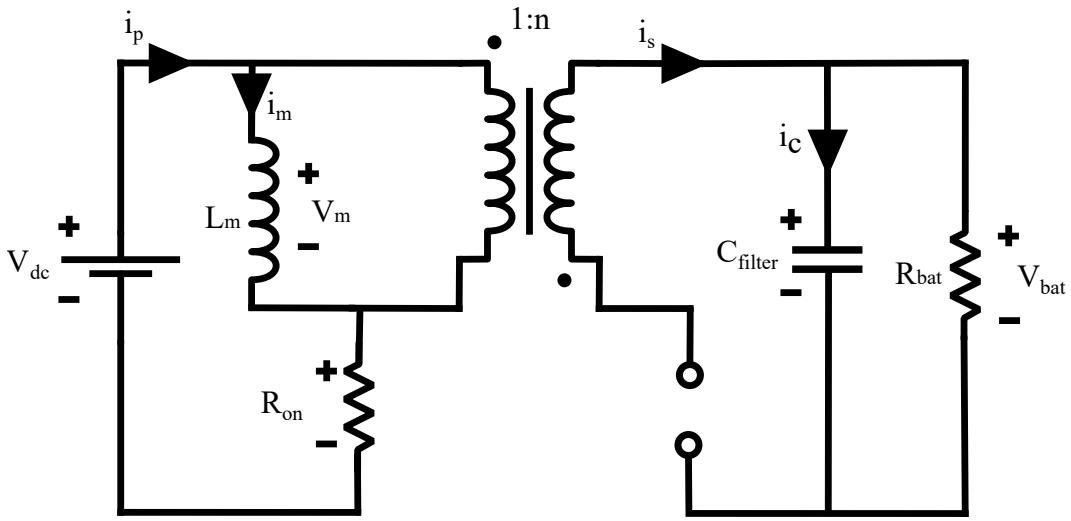

Figure C-1: Flyback converter when Q1 is ON

The second time interval is given when Q2 is ON (duty cycle $D' = 1 - D$), and it is represented in Figure C-2, from where (C.4), (C.5) and (C.3) are extracted.

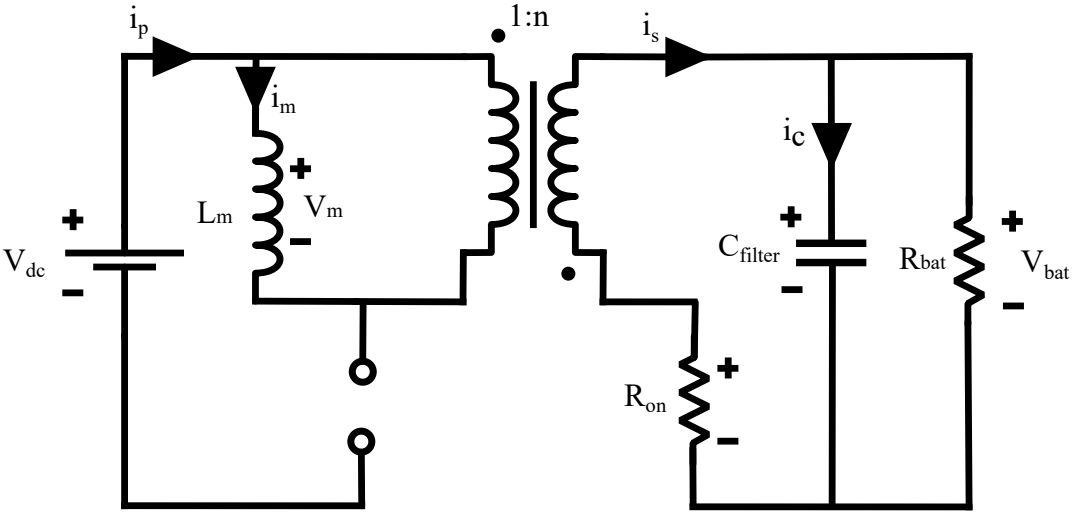

Figure C-2: Flyback converter when Q2 is ON

$$\begin{aligned} & n \cdot V_m(t) = -V_{bat}(t) + V_{R_{on}}(t) \rightarrow \\ & V_m(t) = -\frac{V_{bat}(t)}{n} + \frac{V_{R_{on}}(t)}{n^2} = -\frac{V_{bat}(t)}{n} + \frac{i(t) \cdot R_{on}}{n^2} \end{aligned} \tag{C.4}$$

$$i_c(t) = \frac{i_m(t)}{n} - \frac{V_{bat}(t)}{R_{bat}} \tag{C.5}$$

$$i_p(t) = 0 \tag{C.6}$$

At this point, it is important to take into account that $i_s(t) = i_p(t)/n$.

The next step is to combine both intervals $d(t)$ and $d'(t)$ to average the equations over one switching period. These relationships result in the equations shown in (C.7), (C.8) and (C.9), where $< V_m(t) >= L_m \frac{d < i_m(t) >}{dt}$ and $< i_c(t) >= C \frac{d < V_{bat}(t) >}{dt}$.

$$\begin{aligned} < V_m(t) > = d(t)(< V_{dc}(t) > - < i_m(t) > R_{on}) \\ + d'(t)(-\frac{< V_{bat}(t) >}{n} + \frac{< i_m(t) > R_{on}}{n^2}) \end{aligned} \tag{C.7}$$

$$< i_c(t) >= d(t)(-\frac{< V_{bat}(t) >}{R_{bat}}) + d'(t)(\frac{< i_m(t) >}{n} - \frac{< V_{bat}(t) >}{R_{bat}}) \tag{C.8}$$

$$< i_p(t) >= d(t) < i_m(t) > \tag{C.9}$$

Substituting the equivalents mentioned before in (C.7) and (C.8), the resulting averaged equations are shown in (C.10) and (C.11).

$$\begin{aligned} L_m \frac{d < i_m(t) >}{dt} = d(t)(< V_{dc}(t) > - < i_m(t) > R_{on}) \\ + d'(t)(-\frac{< V_{bat}(t) >}{n} + \frac{< i_m(t) > R_{on}}{n}) \end{aligned} \tag{C.10}$$

$$C \frac{d < V_{bat}(t) >}{dt} = d'(t)(\frac{< i_m(t) >}{n}) - \frac{< V_{bat}(t) >}{R_{bat}} \tag{C.11}$$

As can be seen, (C.9), (C.10) and (C.11) are a nonlinear set of differential equations. Therefore, the next step to construct the small-signal model is to linearize

them.

For that, all averaged signals can be expressed as a DC term plus a small AC variations, as follows in equations from (C.12) to (C.17).

$$d(t) = D + \widehat{d}(t) \tag{C.12}$$

$$d'(t) = D' - \widehat{d}(t) \tag{C.13}$$

$$V_{dc}(t) = V_{dc} + \widehat{v_{dc}}(t) \tag{C.14}$$

$$V_{bat}(t) = V_{bat} + \widehat{v_{bat}}(t) \tag{C.15}$$

$$i_p(t) = I_p + \widehat{i_p}(t) \tag{C.16}$$

$$i_m(t) = I_m + \widehat{i_m}(t) \tag{C.17}$$

With these substitutions, the large-signal averaged inductor equation becomes as shown in (C.18).

$$\begin{aligned} L_m \frac{d(I_m + \widehat{i_m}(t))}{dt} &= (D + \widehat{d}(t))(V_{dc} + \widehat{v_{dc}}(t)) \; - (D + \widehat{d}(t))(I_m + \widehat{i_m}(t)) \cdot R_{on} \\ &\quad - (D' - \widehat{d}(t))(\frac{(V_{bat} + \widehat{v_{bat}}(t)}{n}) \; + (D' - \widehat{d}(t))(\frac{(I_m + \widehat{i_m}(t))}{n^2}) \cdot R_{on} \end{aligned} \tag{C.18}$$

By multiplying and collecting terms, (C.19) is obtained. This equation contains three types of terms [30]. The DC terms contain no time-varying quantities and will be used to implement the average model.

The 1^{st} order terms are linear functions and will be used to implement the small-signal model. The 2^{nd} order terms are functions of the product of the small AC variations and will be assumed to be negligible because their magnitude is much

smaller than the 1^{st} order terms ones.

$$
\begin{aligned}
L_m \frac{d(I_m + \widehat{i_m}(t))}{dt} = & \underbrace{D \cdot V_{dc} - D \cdot I_m \cdot R_{on} - \frac{D' \cdot V_{bat}}{n} + \frac{D' \cdot I_m}{n^2} \cdot R_{on}}_{DC\ terms} \\
& \underbrace{+D \cdot \widehat{v_{dc}}(t) + V_{dc} \cdot \widehat{d}(t) \ - D \cdot R_{on} \cdot \widehat{i_m}(t) - I \cdot R_{on} \cdot \widehat{d}(t)}_{1^{st}\ order\ AC\ terms} \\
& \underbrace{-\frac{D'}{n}\widehat{v_{bat}}(t) + \frac{V_{bat}}{n}\widehat{d}(t) + \frac{D' \cdot R_{on}}{n^2}\widehat{i_m(t)} + \frac{I \cdot R_{on}}{n^2}\widehat{i_m}(t)}_{1^{st}\ order\ AC\ terms} \\
& \underbrace{+\widehat{d}(t) \cdot \widehat{v_{dc}}(t) - R_{on}\widehat{d}(t) \cdot \widehat{i_m}(t) + \frac{\widehat{d}(t) \cdot \widehat{v_{bat}}(t)}{n} - R_{on}\frac{\widehat{d}(t) \cdot \widehat{i_m}(t)}{n^2}}_{2^{nd}\ order\ AC\ terms}
\end{aligned}
\tag{C.19}
$$

Now, in the case of the averaged capacitor, (C.20) is obtained.

$$
C \ \frac{d(V_{bat} + \widehat{v_{bat}}(t))}{dt} = (D' - \widehat{d}(t))(\frac{I_m + \widehat{i_m}(t)}{n}) \ - \frac{V_{bat} + \widehat{v_{bat}}(t)}{R_{bat}} \tag{C.20}
$$

Same as with the inductor equation, by multiplying and collecting terms, the result is shown in (C.21), where there are also three types of terms.

$$
C \ \frac{d(V_{bat} + \widehat{v_{bat}}(t))}{dt} = \underbrace{\frac{D' \cdot I_m}{n} - \frac{V_{bat}}{R_{bat}}}_{DC\ terms} \underbrace{+\frac{D'}{n}\widehat{i_m}(t) - \frac{I_m}{n}\widehat{d}(t) - \frac{\widehat{v_{bat}}(t)}{R_{bat}}}_{1^{st}\ order\ AC\ terms} \underbrace{-\frac{\widehat{d}(t) \cdot \widehat{i_m}(t)}{n}}_{2^{nd}\ order\ AC\ terms} \tag{C.21}
$$

Lastly, for the averaged input current, following the same process, the now linearized terms are shown in (C.22).

$$
\begin{aligned}
I_p + \widehat{i_p}(t) &= (D + \widehat{d}(t))(I + \widehat{i_m}(t)) \\
&= \underbrace{D \cdot I_m}_{DC\ terms} + \underbrace{D \cdot \widehat{i_m}(t) + I_m \cdot \widehat{d}(t)}_{1^{st}\ order\ AC\ terms} \underbrace{+ \widehat{i_m}(t) \cdot \widehat{d}(t)}_{2^{nd}\ order\ AC\ terms}
\end{aligned}
\tag{C.22}
$$

Appendix D

Battery modelling

In order to obtain the first order model of the battery, the most simple way is to apply a current step to the battery and see the response.

To do that, the characteristics of the battery must be known. As explained in Chapter 4, the selected battery is the Bosch PowerPack 300 [26].

The battery mentioned above has the following characteristics in its data-sheet, as shown in Table D.1.

Data	Value
Rated voltage	36 V
Capacity	8.2
Energy	300 Wh

Table D.1: Input data from the Bosch battery datasheet

To do the test, it is necessary one more characteristic that is not specified in the data-sheet: the time response. However, as will be explained further on, this characteristic is used to obtain the open-circuit capacitor, which will not be used in the control strategy (as explained in Chapter 4).Because of that, an arbitrary value close to the typical ones was selected in this thesis.

By entering the aforementioned data into Simulink's battery block, and injecting a current step as an input, the response in Figure D-1 is obtained.

From said figure, the parameters to obtain the first order battery model presented in Chapter 4 in figure 4-13 can be calculated as shown in equations from (D.1) to

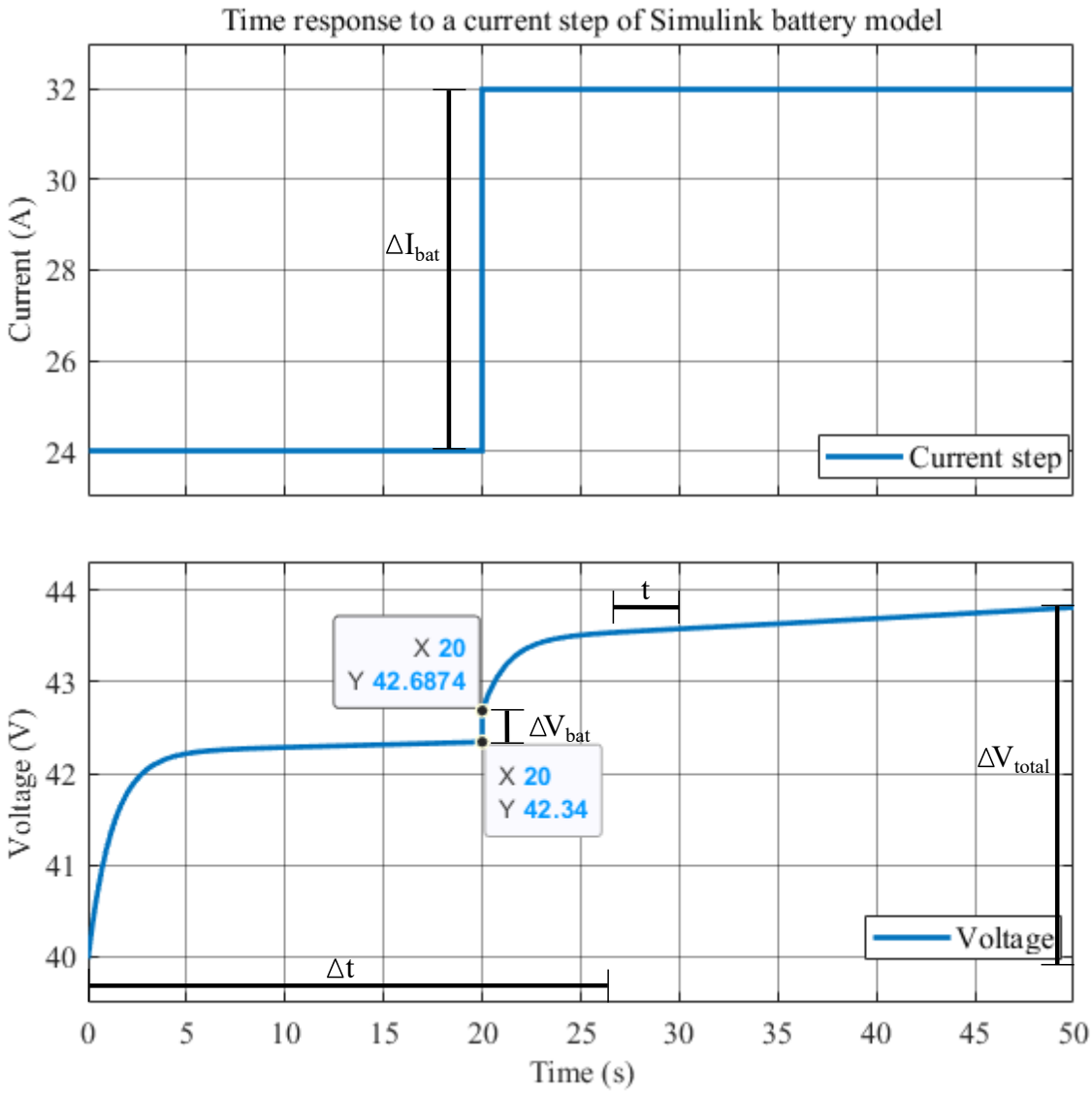

Figure D-1: Time response to a current step: Simulink battery model.

(D.5).

$$R_{ser} = \frac{\Delta V_{bat}}{\Delta I_{bat}} = \frac{0.34}{32 - 24} = 42.5m\Omega \tag{D.1}$$

$$C_{soc} = \frac{I_{bat}}{\frac{\Delta V_{bat}}{\Delta t}} = \frac{32}{\frac{0.34}{26.8}} = 2500F \tag{D.2}$$

$$m_{soc} = \frac{\Delta V_{bat}}{\Delta t} = \frac{0.34}{26.8} = 0.01 \tag{D.3}$$

$$R_{dyn} = \frac{\Delta V_{total} - \Delta V_{bat} - m_{soc}t}{I_{bat}} = \frac{3.2 - 0.34 - 0.01 \times 3.2}{32} = 90m\Omega \tag{D.4}$$

$$C_{dyn} = \frac{t}{3R_{dyn}} = \frac{3.2}{3 \times 90 \times 10^{-3}} = 12F \tag{D.5}$$

With this data, implementing the first order model proposed in Section 4, the response shown in Figure D-2 is obtained. As can be seen, it has almost exactly the same response as the battery.

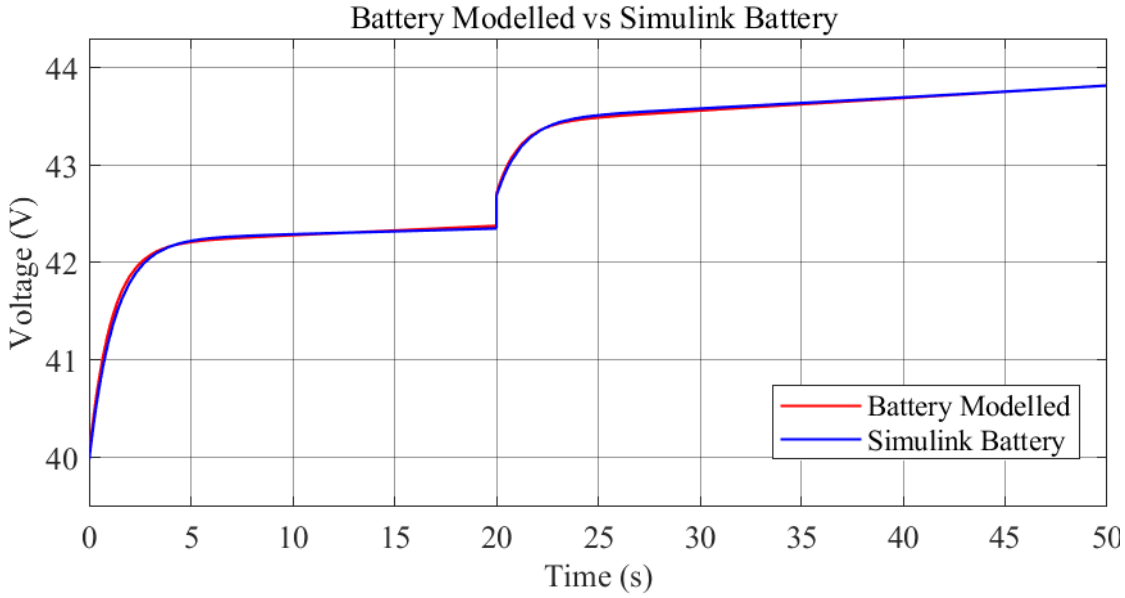

Figure D-2: Time response to a current step: Simulink battery model vs. Modelled Battery.

Acronyms

BW Band-Width. 38

CC Constant Current. 21, 55, 56, 58

CV Constant Voltage. 21, 55, 56, 58

DAB Dual Active Bridge. 25

DER Distributed Energy Resources. 16

e-bike Electric Bicycle. 16

EES Energy Storage Systems. 16

EMI Electromagnetic Interference. 27

EPA Environmental Protection Agency. 13

EV Electric Vehicle. 13, 19

G2V Grid to Vehicle. 22, 48

HP Heat Pumps. 16

LLC Inductor-Inductor-Capacitor. 27

PCC Point of Common Coupling. 16

PEC Power Electronic Converter. 38

PFC Power Factor Correction. 24

PI Proportional Integral. 37, 41

PLL Phase Lock Loop. 5, 41

PR Proportional Resonant. 37, 38

PV Photovoltaic. 15

QoS Quality of Service. 17

QSG Quadrature Signal Generator. 43

SiC Silicon Carbide. 76

SoC State of Charge. 17, 57, 58

SRF Synchronous Reference Frame. 5, 41

V2G Vehicle to Grid. 22, 48

VPP Virtual Power Plant. 20

Bibliography

[1] NASA, "Overview: Weather, global warming, and climate change,"

[2] L. Attanasio, M. Conti, D. Donadel, and F. Turrin, *MiniV2G: An Electric Vehicle Charging Emulator*, vol. 1. Association for Computing Machinery, 2021.

[3] G. B. Moreno and F. D. Project, "The On-Board Charger : Cost and design analysis," 2018.

[4] "Nota de prensa del consejo de ministros del gobierno de españa," 2022.

[5] "Ley 7/2021, de 20 de mayo, de cambio climático y transición energética, boe-a-2021-8447," 2021.

[6] V. T. Tran, D. Sutanto, and K. M. Muttaqi, "The state of the art of battery charging infrastructure for electrical vehicles: Topologies, power control strategies, and future trend," *2017 Australasian Universities Power Engineering Conference, AUPEC 2017*, vol. 2017-Novem, pp. 1–6, 2018.

[7] A. K. Verma, B. Singh, and D. T. Shahani, "Grid to vehicle and vehicle to grid energy transfer using single-phase bidirectional AC-DC converter and bidirectional DC-DC converter," *Proceedings - 2011 International Conference on Energy, Automation and Signal, ICEAS - 2011*, pp. 84–88, 2011.

[8] M. A. Kippke, "Advance Metering Infrastructure for Smart Grid Real Time Energy Management Using Mesh Networks Based on IEEE802 . 15 . 4 and 6LoWPAN," 2020.

[9] J. C. Boemer, D. Brooks, and T. Key, "Recommended settings for voltage and frequency ride through of distributed energy resources," 2015.

[10] EPRI, "Voltage Regulation Support from Smart Inverters," no. December, p. December, 2017.

[11] M. C. Kisacikoglu, B. Ozpineci, and L. M. Tolbert, "EV/PHEV bidirectional charger assessment for V2G reactive power operation," *IEEE Transactions on Power Electronics*, vol. 28, no. 12, pp. 5717–5727, 2013.

[12] O. Turksoy, U. Yilmaz, and A. Teke, "Overview of Battery Charger Topologies in Plug-In Electric and Hybrid Electric Vehicles," *16th International Conference on Clean Energy (ICCE-2018)*, no. September, pp. 1–8, 2018.

[13] A. Khaligh and S. Dusmez, "Comprehensive topological analysis of conductive and inductive charging solutions for plug-in electric vehicles," *IEEE Transactions on Vehicular Technology*, vol. 61, no. 8, pp. 3475–3489, 2012.

[14] S. Islam, A. Iqbal, M. Marzband, I. Khan, and A. Al-Wahedi, "State-of-the-art vehicle-to-everything mode of operation of electric vehicles and its future perspectives," *Renewable and Sustainable Energy Reviews*, vol. 166, p. 112574, 09 2022.

[15] N. Trivedi, N. S. Gujar, S. Sarkar, and S. Pundir, "Different fast charging methods and topologies for ev charging," in *2018 IEEMA Engineer Infinite Conference (eTechNxT)*, pp. 1–5, 2018.

[16] S. S. Zhang, "The effect of the charging protocol on the cycle life of a li-ion battery," *Journal of Power Sources*, vol. 161, no. 2, pp. 1385–1391, 2006.

[17] D. Anseán, M. González, J. Viera, V. García, C. Blanco, and M. Valledor, "Fast charging technique for high power lithium iron phosphate batteries: A cycle life analysis," *Journal of Power Sources*, vol. 239, pp. 9–15, 2013.

[18] A. A. Al-Karakchi, G. Putrus, and R. Das, "Smart EV charging profiles to extend battery life," *2017 52nd International Universities Power Engineering Conference, UPEC 2017*, vol. 2017-Janua, pp. 1–4, 2017.

[19] E. H. El-Zohri and K. Sayed, "Control of EV charging station based on three-phase three-level AC/DC rectifier," *INTELEC, International Telecommunications Energy Conference (Proceedings)*, vol. 2016-Septe, pp. 1–6, 2016.

[20] A. Devices, "Efficient buck-boost converter ideal for power saving modes and wide input voltage ranges,"

[21] X. Ren, Z. Tang, X. Ruan, J. Wei, and G. Hua, "Four switch buck-boost converter for telecom dc-dc power supply applications," in *2008 Twenty-Third Annual IEEE Applied Power Electronics Conference and Exposition*, pp. 1527–1530, 2008.

[22] T. Instruments, "Bidirectional, dual active bridge reference design for level 3 electric vehicle charging stations,"

[23] J. Deng, S. Li, S. Hu, C. C. Mi, and R. Ma, "Design methodology of LLC resonant converters for electric vehicle battery chargers," *IEEE Transactions on Vehicular Technology*, vol. 63, no. 4, pp. 1581–1592, 2014.

[24] E. Çalışkan and O. Ustun, "Smart efficiency tracking for novel switch—llc converter for battery charging applications," *Energies*, vol. 15, p. 1861, 03 2022.

[25] M. K. Kazimierczuk, *Pulse-Width Modulated DC-DC Power Converters*. 2012.

[26] Bosch, "User instructions-user manual-battery,"

[27] R. Components, "Rs components catalog,"

[28] M. Restrepo, J. Morris, M. Kazerani, and C. A. Cañizares, "Modeling and testing of a bidirectional smart charger for distribution system EV integration," *IEEE Transactions on Smart Grid*, vol. 9, no. 1, pp. 152–162, 2018.

[29] K. Corporation, "How to extend ev battery life?," 2022.

[30] R. W. Erickson and D. Maksimović, *Fundamentals of Power Electronics Third Edition*. 2014.

[31] A. Rodríguez, A. Vázquez, D. G. Lamar, M. M. Hernando, and J. Sebastián, "Different purpose design strategies and techniques to improve the performance of a dual active bridge with phase-shift control," *IEEE Transactions on Power Electronics*, vol. 30, no. 2, pp. 790–804, 2015.